Acta Materialia 157 (2018) 339–354

Contents lists available at ScienceDirect

Acta Materialia

journal homepage: www.elsevier.com/locate/actamat

Full length article

Explicit modeling of double twinning in AZ31 using crystal plasticity finite elements for predicting the mechanical fields for twin variant selection and fracture analyses

Milan Ardeljan, Marko Knezevic*

Department of Mechanical Engineering, University of New Hampshire, Durham, NH, 03824, USA

ARTICLE INFO

Article history:
Received 3 April 2018
Received in revised form
27 June 2018
Accepted 19 July 2018
Available online 23 July 2018

Keywords:
Twinning
Microstructures
Crystal plasticity
Finite elements
Magnesium alloys

ABSTRACT

A number of studies have found that the formation of double twins in low symmetry metals can lead to the onset of strain localizations, leading further to void nucleation and ultimately fracture. This work extends a recently developed three-dimensional crystal plasticity finite element framework [1] to explicitly model kinematics and kinetics of nucleation/formation, propagation, and thickening/growth of a discrete double twin lamella ($\{10\bar{1}1\}-\{10\bar{1}2\}$) in a magnesium alloy AZ31. With this approach, morphological and crystallographic reorientations as well as the shear transformation strains associated with strain accommodation by the double twinning sequence are modeled during simple compression and tension. The simulations predict that the distribution of local stress-strain fields during formation and growth of primary contraction twin creates the driving force for the formation of a secondary extension twin variant, which is consistent with experimental observations in both compression and tension. In particular, the contraction twin variant $(0\bar{1}11)[0\bar{1}1\bar{2}]$ is predicted to form an internal extension twin variant $(01\bar{1}2)[0\bar{1}11]$. Furthermore, the prediction of the underlining crystallographic slip deformation mechanism reveals a substantial activity of basal slip within the contraction portion of the double twin, causing strain localization in its vicinity. Finally, the simulations reveal a gradient in the traction force field across twin-parent interface, suggesting that contraction twin-parent boundaries are weak links in the microstructure where voids can nucleate.

1. Introduction

Magnesium (Mg) alloys are attractive structural materials for various automotive and aerospace applications due to their light weight and high strength to weight ratio [2,3]. However, their ductility is limited, which leads to low formability and premature failure at room temperature [4]. Furthermore, magnesium alloys display strong mechanical anisotropy, which is another major hurdle to their widespread use in design and manufacturing [5–8]. Plastic deformation in polycrystalline metals is most often accommodated by plastic slip, but under certain circumstances it can be carried by both twinning and slip. Mg is a hexagonal close packed (HCP) metal which deforms profusely by twinning in order to accommodate strain along the crystallographic **c**-axis. It is thought that the main reason for the lack of ductility of magnesium alloys is the development of $\{10\bar{1}1\}-\{10\bar{1}2\}$ double twins, which promote early shear failure by localized void formation and propagation [9,10]. A significant amount of research has been carried out into suppressing the development of contraction and double twins in this class of metals by alloying and grain size reduction/refinement [11–16].

In Mg alloys, the easiest slip mode is basal slip, although prismatic and pyramidal slip systems also operate [17–20]. The most common active twin modes in Mg alloys are extension $\{10\bar{1}2\}\langle 10\bar{1}1\rangle$ and contraction $\{10\bar{1}1\}\langle 10\bar{1}2\rangle$ modes, where the former facilitates extension and the latter facilitates contraction along the crystallographic **c**-axis [21–24]. The *c/a* ratio for Mg is 1.624 [25], which is less than the ideal $\sqrt{8/3}\cong 1.633$ for HCP crystal structure. The tension twin mode is easy to activate by applied **c**-axis tension deformation. Therefore, many experimental reports on various magnesium alloys have shown that extension twins can grow quickly and form thick lamellae, and even encompass the

* Corresponding author. University of New Hampshire, Department of Mechanical Engineering, 33 Academic Way, Kingsbury Hall, W119, Durham, NH, 03824, United States.
E-mail address: marko.knezevic@unh.edu (M. Knezevic).

https://doi.org/10.1016/j.actamat.2018.07.045
1359-6454/

whole grain, and generally reach profuse levels without failing the material [26,27]. In order to accommodate applied strain by activating this type of twinning, crystal structure reorients by 86° around $\langle 1\bar{2}10\rangle$ axis. Overall, these twins can improve ductility, but they lower the strength, due to their relatively low resistance to strain in the twinned orientation. On the other hand, contraction twins cause crystal to reorient by 56° around $\langle 1\bar{2}10\rangle$ axis. These twins usually remain very thin and nucleate further a second extension twin inside their domain that often expands very quickly, overtaking most of the contraction twin lamella. As a result, the so-called double twin is formed. It has been experimentally observed that during lateral growth of secondary extension $\{10\bar{1}2\}$ twins, the final $\{10\bar{1}1\}-\{10\bar{1}2\}$ double twin shape is largely enforced by the shape of the primary contraction $\{10\bar{1}1\}$ twin [28,29].

Experimental characterization of AZ31 samples deformed in tension has been carried out by using transmission electron microscopy. This revealed that **c**-axis contraction was accommodated predominantly by the formation of $\{10\bar{1}1\}-\{10\bar{1}2\}$ double twins, causing 37.5° $\langle 1\bar{2}10\rangle$ and 30.1° $\langle 1\bar{2}10\rangle$ twin/matrix reorientations [29]. This work reported the presence of microcracks at the double-twin intersections and locally along the double-twin/matrix interfaces, suggesting that the double-twin formation in polycrystalline Mg alloys promote early shear failure due to localized void formation. In the same work, visco-plastic self-consistent (VPSC) crystal plasticity simulations were employed to aid the interpretation of the obtained results, but the model was unable to fully capture the observed double twinning sequences. Another study [30] sought to explain the nucleation of the secondary twin at the primary twin interface and its early stages of growth in the primary twin domain. The study concluded that the experimentally observed double twinning sequences [29] were more energetically favorable than other sequences.

In many studies [10,21,29,31–34], the formation of double twins has been correlated to void and crack formation and flow localization in the vicinity of its boundaries. This correlation has been rationalized to arise due to substantial crystal reorientations associated with the double-twinned region and underlining shifts in active crystallographic slip modes. The twin introduces a new crystallographic orientation into the grain and within this domain favorable slip systems may differ from those in the parent. The twinned region of a contraction twin is much more favorably oriented for easy basal slip than the original parent crystal [30]. The intense basal slip activity that results within the thin lamella region of the double twin produces a localized shear that cannot be accommodated across the primary twin interface and ultimately leads to void formation. A recent investigation of twinning in a Mg-4wt%Li alloy [35], indicated that the lack of plastic relaxation mechanisms causes void formation, especially at the tips of double twin/grain boundary junctions under a complex stress state.

Reference [36] presented an analysis of transgranular fracture in hot rolled AZ61, which was subjected to a triaxial stress state at the vicinity of a notch by combining EBSD and Schmid's law numerical calculations. Examination of the misorientation boundaries between parent and twin regions revealed a strong influence of $\{10\bar{1}1\}-\{10\bar{1}2\}$ double twinning on the formation of transgranular micro-cracks. The study also revealed that this twinning mode amplifies the shear stresses projected on the basal systems, resulting in early shear localization and transgranular void/crack initiation.

A number of characterization studies showed that the texture changes caused by twinning are the main cause of the observed macroscopic stress–strain anisotropy of HCP metals. In the predominantly slip dominated deformation curves, the hardening rate decreases with applied strain, while in the twinning and slip dominated deformation curves, there are inflection points in the hardening rate, where the hardening rate increases with applied strain [8,37,38]. However, the evolution of internal stresses, in a localized stress field in subsets of grains is complex and more challenging to measure. Crystallographic details of a twin can locally affect slip activity and hence influence the macroscopic stress-strain response. Moreover, the crystallographic boundaries introduced by twins can pose obstacles to slip motion, resulting in hardening effects. Finally, twin morphology can arise through the local stress states that are generated within the twin and the surrounding matrix. In addition to creating localized hardening, the localized stress-strain fields produced by twins, also influence the local slip activity within the parent grain and twin itself. They also have an effect on formation of additional twins, and twin expansion rates [39]. Knowledge of these local fields can help explain the probability of other twin-governed phenomena, such as secondary twinning and de-twinning [40–42].

The most common crystal plasticity models for metals that deform by a combination of slip and twinning, utilize polycrystal homogenizations, such as Taylor-type [43–46] or self-consistent [47–50]. In these approaches, the grain neighborhood is homogenized and hence the grain boundaries and grain neighbors are not explicitly modeled. Such schemes assume homogeneous stress states in the matrix and twin phases, which can be expected to be very different from the actual highly localized stresses produced by twin domains, as have been reported experimentally using techniques such as far-field 3D-XRD [39,51–53] and differential-aperture X-ray microscopy (DAXM) [54]. Localized stresses as a result of twins can be calculated using spatiotemporal models such as phenomenological models within FE [55,56], fast Fourier transform crystal plasticity [57], and crystal plasticity finite element (CPFE) [58–63]. These techniques can calculate the spatially resolved mechanical fields within deformed microstructures, and overcome the limitations of the polycrystal homogenization techniques [64].

In this work, a recently developed crystal plasticity model that explicitly models a twin lamella in 3D in the FE framework [1] is extended to model secondary twin lamellae. The underlying crystal plasticity constitutive model considers both anisotropic elastic and plastic behavior of the material. The implemented hardening law is a function of strain, temperature and strain rate [65], and it is governed by the thermally activated dislocation density evolution on three considered slip modes: basal **a**, prismatic **a** and pyramidal $\mathbf{c}+\mathbf{a}$. In order to form a $\{10\bar{1}1\}-\{10\bar{1}2\}$ explicit double twin lamella in a parent grain under a plastic deformation condition, either simple compression or tension is applied to form a primary contraction twin lamella, which after additional straining forms a secondary extension twin lamella within its region. The work begins by examining whether the present full-field approach can predict the most commonly observed double twinning sequence, because such predictions are essential for predicting the local mechanical fields. Unlike in a Schmid analysis, the present approach was found successful in predicting the most commonly observed double twinning sequence in both tension and compression. Next, the slip analysis within these regions of interest is performed to determine what slip modes are prevalent. While the formation of an extension twin within an existing twin lamellae is the easiest, basal slip was found to operate more in the remaining portion of the contraction lamellae than within the secondary extension twin. Finally, the influence of double twinning on the localized stress-strain fields across the granular structure in the vicinity of double twin formation is investigated. The simulations reveal a gradient in the field across the twin-parent interface suggesting that contraction twin-parent boundaries are locations in the microstructure, where voids can nucleate.

2. Modeling framework

In this section, the main relationships and stages involved in a multi-level modeling framework are presented. Fig. 1 displays the modeling framework. Going from left to the right side (frames a-c), the material length magnifies/increases and each frame represents a specific instance at which the material response is being evaluated. At the coarsest level (frame a), the material response of a polycrystal, which is in the form of a granular microstructural model is considered through the use of the finite element (FE) homogenization method. As a full-field model, this method fulfills both stress equilibrium and strain compatibility conditions making it one of the best modeling tools for capturing realistic interactions between the constituent grains. Each grain in the polycrystal is represented by an element set, which discretizes a given grain into finite elements (frame b). At this length scale, at each FE integration point, a material constitutive response is estimated using crystal plasticity theory. It assumes that the strain is being accommodated in the material by simultaneous action of crystallographic slip and deformation twinning. The latter is accomplished using the pseudo slip model [66–68], which estimates the amount of accommodated shear strain on a particular twin variant plane. Once the prescribed critical twin volume fraction value of a particular twin system is achieved, the twin lamella(e) within the grain are explicitly modeled, by reorienting the lattice and enforcing the characteristic twin shear. More details about this stage in the modeling procedure are given and discussed in the next section.

In order to determine the single crystal response at each integration point a User MATerial (UMAT) subroutine based on crystal plasticity constitutive formulation was used in Abaqus Standard. The framework facilitates various loading conditions from low to high level of complexity that can be applied in the form of suitable boundary conditions. This applied load is divided into time/strain increments, where for each increment a global stress equilibrium solution is found using a numerically iterative procedure of the finite element method. This is achieved by solving Eq. (1), which represents the nonlinear FE governing equation in its linearized form:

$$\left(\int_V \mathbf{B}^T \mathbf{J} \mathbf{B} dV\right) \Delta \mathbf{U} = \mathbf{R} - \int_V \mathbf{B}^T \boldsymbol{\sigma} dV. \tag{1}$$

In this relation, the listed quantities are respectively **B** - finite element strain-displacement matrix, **J** - material Jacobian matrix, $\Delta\mathbf{U}$ - displacement increment solution, **R** - applied force vector and $\boldsymbol{\sigma}$ - Cauchy stress tensor [69–71].

Next, the key equations pertaining to the crystal plasticity constitutive law are briefly described in order to relate the material stress to material distortion (stretch plus rotation) at each integration point within each finite element in the model [72–74]. A standard continuum mechanics notation is used, where tensors are denoted using roman boldface symbols, while scalars are italicized and not boldfaced. To denote a time derivative we place a dot over particular quantity.

2.1. Kinematics of slip and twinning within CPFE

The total velocity gradient tensor, **L**, can be additively decomposed as following:

$$\mathbf{L} = \mathbf{L}^e + \mathbf{L}^p, \tag{2}$$

where $\mathbf{L}^e$ and $\mathbf{L}^p$ represent elastic and plastic velocity gradients, respectively. The plastic part of the velocity gradient contains the contributions from both slip and twinning via

$$\mathbf{L}^p = \mathbf{L}^{sl} + \mathbf{L}^{tw}. \tag{3}$$

The corresponding contributions to the velocity gradients, due to slip and twinning, are further expressed as:

$$\mathbf{L}^{sl} = \sum_{\alpha}^{N^{sl}} \dot{\gamma}^{\alpha} \mathbf{m}_o^{\alpha} = \sum_{\alpha}^{N^{sl}} \dot{\gamma}^{\alpha} \mathbf{b}_o^{\alpha} \otimes \mathbf{n}_o^{\alpha}, \quad \mathbf{L}^{tw} = \sum_{\beta}^{N^{tw}} \dot{f}^{\beta} S^{\beta} \mathbf{m}_o^{\beta} = \sum_{\beta}^{N^{tw}} \dot{f}^{\beta} S^{\beta} \mathbf{b}_o^{\beta} \otimes \mathbf{n}_o^{\beta}, \tag{4}$$

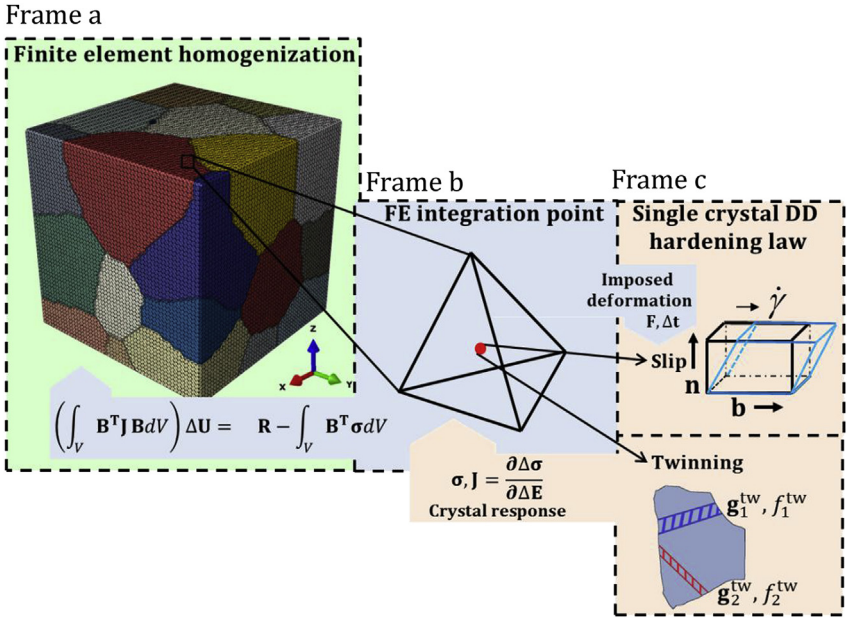

Fig. 1. Schematic of the multi-level modeling framework.

where $\dot{\gamma}^{\alpha}$ stands for the shearing rate on the particular slip system α, $\mathbf{m}_o^{\alpha}$ and $\mathbf{m}_o^{\beta}$ represent Schmid tensors associated with slip system α and twin system β, respectively, S^{β} denotes the value of characteristic twin shear accompanied to twinning. Finally, N^{sl} and N^{tw} represent the total number of available slip and twin systems, respectively. The Schmid tensors represent the unit slip or twin system tensor, defined as the dyadic product ($\otimes$) between the unit Burgers direction ($\mathbf{b}_o$) and unit plane normal ($\mathbf{n}_o$) vectors of slip system α or twin system β, respectively, in the undeformed configuration indicated by subscript 'o'.

In order to determine the rate of change of the twin volume fraction per each particular twin system ($\dot{f}^{\beta}$), the pseudo-slip model takes under consideration only the shear strain accommodated by twinning and not the morphological and crystallographic reorientation of a twin domain. The latter two are explicitly modeled, as described shortly. The relationship between the $\dot{f}^{\beta}$ and the shear rate on the twin system ($\dot{\gamma}^{\beta}$) is inversely proportional to the characteristic shear strain [66,67]:

$$\dot{f}^{\beta} = \frac{\dot{\gamma}^{\beta}}{S^{\beta}}. \tag{5}$$

Due to integration, in a given strain increment, previous equation becomes:

$$\Delta f^{\beta} = \frac{\Delta\gamma^{\beta}}{S^{\beta}}. \tag{6}$$

Integrating over n strain increments, the accumulated twin volume fraction of a particular twin system, β, can reach unity (i.e. $\sum_1^n \Delta f^{\beta} = 1$), which means that the particular twin system accommodated the maximum possible amount of shear strain (i.e. $S^{\beta} = \sum_1^n \Delta\gamma^{\beta}$). In this case, the whole volume of the given parent grain completely reoriented into the twin variant β. Therefore, physically it is not possible to have any other twin variant active in this particular grain. In contrast, if multiple twin variants activate in a given grain then none of them can rich a volume fraction of unity but only sum of their volumes can rich unity.

In our approach, we use a finite deformation formulation, in which an assumption is made that the deformation gradient ($\mathbf{F}$) can be multiplicatively decomposed in its elastic ($\mathbf{F}^e$) and plastic ($\mathbf{F}^p$) contributions as:

$$\mathbf{F} = \mathbf{F}^e\mathbf{F}^p, \tag{7}$$

where elastic component contains contributions to the deformation gradient due to both elastic stretching and lattice rotation, while the plastic component relates contributions to deformation gradients due to plastic deformation. The constitutive relationship between $\mathbf{F}^e$ and stress in the crystal is made as:

$$\mathbf{T}^e = \mathbf{C}\mathbf{E}^e, \quad \mathbf{T}^e = \mathbf{F}^{e^{-1}}\{(det\mathbf{F}^e)\boldsymbol{\sigma}\}\mathbf{F}^{e^{-T}}, \quad \mathbf{E}^e = \frac{1}{2}\left\{\mathbf{F}^{e^T}\mathbf{F}^e - \mathbf{I}\right\}, \tag{8}$$

where $\mathbf{T}^e$ is the second Piola-Kirchhoff stress tensor and $\mathbf{E}^e$ is the Lagrangian finite strain tensor, both representing a pair of work conjugate stress and strain measures, $\mathbf{C}$ is the fourth-order elasticity tensor and $\boldsymbol{\sigma}$ is the Cauchy stress in the crystal. To compute stress, we need to evaluate the evolution of $\mathbf{F}^p$ which is ultimately determined by crystallographic slip and twinning (microshear rates) and it can be expressed in a rate form using the following flow rule relationship:

$$\dot{\mathbf{F}}^p = \mathbf{L}^p\mathbf{F}^p. \tag{9}$$

If we integrate Eq. (9) from t to $\tau = t + \Delta t$ it becomes:

$$\mathbf{F}^p(\tau) = \exp(\mathbf{L}^p\Delta t)\mathbf{F}^p(t). \tag{10}$$

Furthermore, the exponential can be conveniently approximated and further expanded using Eq. (3) as:

$$\mathbf{F}^p(\tau) = \{\mathbf{I} + \Delta t\mathbf{L}^p\}\mathbf{F}^p(t) = \left\{\mathbf{I} + \Delta t\left(\mathbf{L}^{sl} + \mathbf{L}^{tw}\right)\right\}\mathbf{F}^p(t), \tag{11}$$

where $\mathbf{I}$ is the identity matrix.

Moreover, we can rewrite previous equation as:

$$\mathbf{F}^{p^{-1}}(\tau) = \mathbf{F}^{p^{-1}}(t)\left\{\mathbf{I} - \Delta t\left(\mathbf{L}^{sl} + \mathbf{L}^{tw}\right)\right\}. \tag{12}$$

Next, we write $\mathbf{L}^{tw}$ as a summation of two parts:

$$\mathbf{L}^{tw} = \mathbf{L}^{tw,pts} + \mathbf{L}^{tw,ots}, \tag{13}$$

where $\mathbf{L}^{tw,\,pts}$ denotes the velocity gradient of the most active twin variant, which we will be referencing further in the paper as the predominant twin system (*pts*) and $\mathbf{L}^{tw,\,ots}$ which denotes the velocity gradient from all other twin systems contributing to plasticity.

2.2. Kinetics of the slip and twinning mechanism

In order to accurately estimate the shear strain rates, $\dot{\gamma}^{\alpha}$ and $\dot{\gamma}^{\beta}$, that can be accommodated on each slip system α and twinning system β, respectively, we use a well establish power-law relationship to compare the resolved shear stress value ($\tau^{\alpha} = \mathbf{T}^e\cdot\mathbf{m}_0^{\alpha}$ for slip and $\tau^{\beta} = \mathbf{T}^e\cdot\mathbf{m}_0^{\beta}$ for twinning) on the system to their corresponding critical resistance value τ_c^{α} for slip systems and τ_c^{β} for twin systems [67,75,76]:

$$\dot{\gamma}^{\alpha} = \dot{\gamma}_0\left(\frac{|\tau^{\alpha}|}{\tau_c^{\alpha}}\right)^{\frac{1}{m}} sign(\tau^{\alpha}), \quad \dot{\gamma}^{\beta} = \begin{cases} \dot{\gamma}_0\left(\dfrac{|\tau^{\beta}|}{\tau_c^{\beta}}\right)^{\frac{1}{m}} sign\left(\tau^{\beta}\right) & if\ \tau^{\beta} > 0 \\ 0 & if\ \tau^{\beta} < 0 \end{cases} \tag{14}$$

where $\dot{\gamma}_0$ is a reference slip rate (arbitrarily taken here as 0.001 s^{-1}) and m denotes the strain rate sensitivity factor (taken here to be 0.02 for both slip and twinning systems).

The hardening law used to govern evolution of τ_c^{α} and τ_c^{β} is presented in Ref. [77], and it is based on the evolution of dislocation density (DD). In the model, dislocations are stored according to a thermally activated rate law in which the resistances τ_c^{α} and τ_c^{β} are a function of strain, temperature, and strain rate [65,78]. These relationships are provided in appendix A for completeness of the present paper. The material parameters for AZ31 utilized in the present model are taken from Ref. [77].

3. Explicit incorporation of twin lamella in CPFE

3.1. Finite element model of granular microstructure

In order to create a polycrystal (e.g. Fig. 1a) represented by a cluster of equiaxed grains, a procedure for generation of synthetic granular microstructure is necessary. In this work, the 3D synthetic voxelized microstructure and surface meshes for the grain boundaries were generated in the publicly available software DREAM.3D (Digital Representation Environment for the Analysis of

Materials in 3D) [79,80]. The software generates 3D voxel-based granular microstructure and surface meshes for each individual grain based on a specified grain size and grain shape distributions. It is also important to mention that DREAM.3D performs a Laplacian based smoothing filter on the voxelized granular microstructure to suppress and remove jagged boundaries between grains which again contributes to better grain representation. A surface mesh consists of triangular elements and represents an important link between a voxel-based model on one side and a volumetric (in our case tetrahedral) 3D mesh on the other side. Hence, starting from individual grain surface meshes, obtained from DREAM.3D, we developed a meshing procedure to acquire their 3D solid meshes securing mesh conformance between the grain boundaries. This 3D meshing is performed within Patran and the reader can find a more elaborate step-by-step description of it in Refs. [81,82]. As a final result of this meshing procedure, we obtain a FE model of the granular microstructure used in this study. All relevant details concerning the model are provided in the next section (Fig. 3).

3.2. Procedure of discrete double twin lamella modeling

In this section, the main steps involved in the procedure for explicit incorporation of twin lamella in FE framework are summarized. A reader can find a more in depth explanation of it in Ref. [1], where this procedure was developed for the first time. The procedure was later used for explicit formation and thickening of an extension twin lamellae in AZ31 and, in particular, for revealing the effect of dislocation density-twin interactions on twin growth [83]. The purpose of this study is to explicitly model and investigate a double twin lamella formation in AZ31. The double twin is created within a parent grain by the formation of a primary contraction twin lamella first and then formation of a secondary extension twin lamella within the primary twinned region. This double twin formation is achieved by applying external deformation on the granular microstructure in the form of consecutive deformation steps. The deformation had to be interrupted at specific strain levels in order to alter the FE mesh for the twin formation. Fig. 2 facilitates an explanation of the procedure. It shows a brief summary of all intermediate steps necessary to form a twin lamella within the chosen parent grain.

The integrated modeling tool set consists of a master Matlab script that handles post-processing of the deformed granular mesh before and after twin lamella formation and can generate the appropriate Patran and Python scripts necessary for performing geometric manipulations and mesh generations. To make this whole procedure as automated as possible, we highly exploited the scripting capabilities of the above mentioned software packages (Matlab, Patran, Python). We execute Patran scripts within Patran, the FE preprocessor from MSC Software, to carry out surface and 3D meshing of individual granular structures once the twin lamella is instantiated. On the other hand, Python scripts are used within Abaqus to obtain individual surface grain meshes from the deformed solid granular model (after deformation step is applied) and in the process of mesh cleanup, where bad aspect ratio triangular elements are collapsed before solid meshing of grains in 3D.

After a deformation step (e.g. in simple compression) is accomplished to a prescribed strain level (Fig. 2a), the procedure starts by obtaining the deformed surface meshes of all individual grains (Fig. 2b). Next, we want to introduce a twin lamella into the parent grain. At this step, the predominant twin system (*pts*) and exact location of the twin lamella in the parent grain are determined, which will be described later. Hence, based on the predominant twin system we can uniquely define in 3D two twin planes with specified mutual distance between them (Fig. 2c). This distance should account for the incremental increase in twin volume that accumulated in the previously performed deformation step. The Matlab script identifies all intersection points between these two twin cutting planes and the 3D surface mesh of the parent grain (Fig. 2d). Next, the Patran script uses the coordinates of these points to reconstruct the closed loops that define each of the two intersected planes and to mesh them with triangular elements of similar size to the ones used to build the surface mesh of the intersected (parent) grain. After meshing is done, the intersection plane surface meshes are exported, which are then used to construct new parent and twin grain surface meshes (Fig. 2e). Finally, a Python script performs a mesh cleanup by collapsing any element with aspect ratio greater than 4 in the granular microstructure. This automated procedure is applied after completion of each deformation step every time when a new twin lamella has to

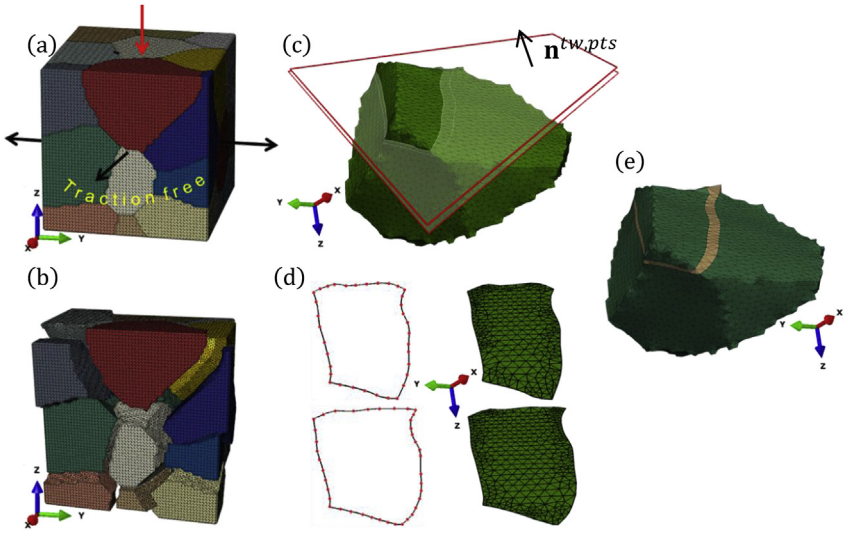

Fig. 2. Procedure for explicit incorporation of twinning in CPFE: (a) An example deformation step of simple compression; (b) Exploded surface meshes of individual grains upon deformation; (c) Intersection between the two twin cutting planes and the 3D surface mesh of the parent grain developing the twin; (d) Two contours composed of intersection points connected by a line used to obtain two meshed twin intersected planes; (e) Resulting twin-parent grain mesh.

be formed or thickened for a prescribed volume increment. As a final outcome, at the end of this procedure we get a twin lamella of a desired volume instantiated into a parent grain with conformal grain boundaries within the granular model.

While performing the above-mentioned procedure, we minimize as much as possible the changes made to the granular model mesh away from the formed twin lamella region. After meshing the interior of the grains and completing the procedure, in order to transfer the deformation state of all grains in the model from previous step and to use it in the subsequent deformation step, we map the following state variables from the old mesh (before twin lamella instantiation) to the new mesh (after twin lamella instantiation): $\mathbf{F}^p$ – plastic deformation gradient, dislocation densities and crystal orientations (keeping any developed intra-grain misorientations due to the previous deformation). We map the values of the state variables between the finite elements in the "old" mesh (before applying any alterations to the mesh) and the "new" mesh (after instantiating the twin) based on mutual proximity of their centroids. This element mapping/matching is performed for each grain within the granular model.

From the experimental records it can be inferred that the twin nucleation sites can be usually found at grain boundaries at specific points of highest stress concentration. Hence, the initial location of the primary contraction twin lamella in both cases of simple compression and tension is determined by applying this criterion and examining the von Mises stress contours over the entire volume of the model.

3.3. Accommodation of the characteristic twin shear by twin lamella

Thus far, we described how the morphological and crystallographic reorientation of the twin lamella is handled in our explicit twin modeling approach. Based on a pseudo-slip model and the total accumulated twinning activity a discrete twin lamella of appropriate volume is explicitly formed. However, in order to fully model all aspects of twinning necessary to accurately predict the mechanical fields, we also have to account for the accommodation of the characteristic twinning shear within the reoriented twinned volume. As a result, the accommodated plastic strain by the twin corresponds to its size. Here, we describe the necessary steps that have to be performed in between deformation steps to satisfy the kinematics and kinetics pertaining to the twin shear strain, which influences the mechanical behavior of the parent and twin grain before and after the twin lamella is formed.

When the twin lamella is explicitly introduced, regardless of whether it is a primary or secondary lamella, deformation history is changed locally. This is achieved by modifying plastic deformation gradient ($\mathbf{F}^p$) and enforcing the appropriate value at each integration point within each finite element belonging to these two regions. In the twinned region, we enforce the values of $\mathbf{F}^p$ to be:

$$\mathbf{F}^{p^{-1}}(\tau) = \left\{\mathbf{I} - S^{tw,pts}\mathbf{m}_0^{tw,pts}\right\}, \tag{15}$$

while in the parent grain this value is altered according to:

$$\mathbf{F}^{p^{-1}}(\tau) = \mathbf{F}^{p^{-1}}(t)\left\{\mathbf{I} + f^{tw,pts}S^{tw,pts}\mathbf{m}_0^{tw,pts}\right\}. \tag{16}$$

Equations (15) and (16) are special cases of Eq. (12), with Eq. (15) restricted to the twinned region of the 'pts' twin variant and Eq. (16) restricted to the parent grain containing the twin variant. The accumulated twin volume fraction is denoted with $f^{tw,pts}$, where the superscript denotes the variant $\beta = tw, pts$ that has been selected as previously mentioned predominant twin variant system. These two equations (Eq. (15) and (16)) ensure the transfer of strain between the parent and twin grain. While the twin accommodated the plastic strain solely corresponding to its size, any strain accommodated by the slip is transformed to the parent. To be more specific, Eq. (15) assigns the appropriate amount of strain that has been accommodated by the predominant twin variant (*pts*) to the twin volume, while Eq. (16) ensures that this same amount of strain is deleted from the parent grain. In order to enforce these two equations and retain the numerical stability at the same time, the value of $\mathbf{F}^p$ is multiplicatively decomposed and then updated during much smaller strain (or time) increments at the beginning of each subsequent deformation step. Once the characteristic twin shear transfer is successfully accomplished between the parent and the twin grain, simple compression (or tension) boundary conditions are enforced in order to perform next deformation step to further strain the grain model.

4. Double twinning in AZ31

4.1. Finite element model set up

Fig. 3 shows the final FE mesh of the granular microstructure used in this work. Also shown are the two cut plane views with consistent grain coloring map, where the model is cut in half to expose the interior of the granular microstructure (two right-most images in Fig. 3).

The created FE model consists of 29 grains in total and approximately 570,000 tetrahedral finite elements (type C3D4 - continuum 3D four nodal). Very fine FE resolution/density is applied, where each grain is discretized with roughly 19,500 finite elements in order to accurately capture inhomogeneity as best as possible in the deformation fields. All grains in the polycrystal can deform by twinning using the pseudo-slip model, but for the sake of simplicity, we perform explicit modeling of twin lamella for the central grain only. We select the grain positioned in the center of the model which is surrounded by the highest number of grains (colored in green in the two right-most images in Fig. 3) to form a $\{10\bar{1}1\} - \{10\bar{1}2\}$ double twin. We consider two different deformation modes/cases. The double twin is formed within the central (parent) grain by deforming the granular model, firstly by applying simple compression along the z-axis and secondly by applying simple tension along the y-axis. We arbitrarily allocate crystal orientations in the model for all grains except for the central one, where specific crystal orientation $(0^\circ, 350^\circ, 0^\circ)$, expressed in Bunge-Euler convention, has been assigned for both compression and tension case. This starting crystal orientation is favorable for $\{10\bar{1}1\}$ contraction twinning for the corresponding deformation cases. Finite elements within any particular grain (element set) share the same crystal orientation. Hence, each grain possesses initial intragranular misorientation of zero degrees. It should be noted that in the tension case, in order to favor contraction twinning over prismatic slip, we lowered the temperature. Hence, deformation in simple tension was simulated at a temperature of 70 K.

The simple compression boundary conditions are prescribed by specifying a displacement of the top surface in the negative z-direction, while enabling the lateral sides to be traction-free and constraining the bottom surface in z-direction. Following the same pattern, simple tension boundary conditions were prescribed by displacing the right surface of the model along the positive y-direction. In both deformation cases (compression and tension) a double twin was formed in the central grain after applying three consecutive deformation steps (stages of remeshing). In the first stage, the grain model was pre-strained in simple compression to a true strain of 0.073, which was necessary for the parent grain to

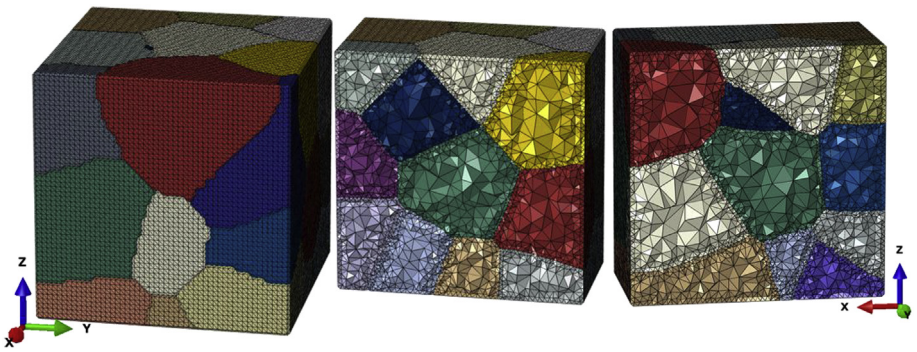

Fig. 3. FE model of explicit grain structure composed of 29 grains and approximately 570,000 C3D4 finite elements. The model is sectioned in two directions to show the interior of the granular model, where the initial crystal orientation of the central grain (colored in green) is chosen to be favorable for $\{10\bar{1}1\}10\bar{1}2$ contraction twinning. (For interpretation of the references to color in this figure legend, the reader is referred to the Web version of this article.)

generate a primary $((0\bar{1}11)[0\bar{1}1\bar{2}])$ contraction twin lamella of sufficient volume. This lamella is afterwards explicitly formed. In the subsequent deformation stage, the grain model was deformed for additional true strain of 0.056, in order to nucleate a secondary $((01\bar{1}2)[0\bar{1}11])$ extension twin within the existing primary twin lamella domain. In the third and final deformation stage, the grain model, which now contains the double twin, was deformed for a small additional true strain of 0.015 in order to better reach the equilibrium state after forming the secondary twin and establish stress-strain fields across the volume. These strain increments correspond to the compression case, while the strains at each stage for the simple tension case are 0.118, 0.061 and 0.015 respectively. In tension, the same double twin variant sequence $(0\bar{1}11)[0\bar{1}1\bar{2}] - (01\bar{1}2)[0\bar{1}11]$ is predicted as the most favorable. The volume fractions of the primary contraction twin lamellae are 1.5% (compression case) and 1.3% (tension case) of the parent grain volume. The percent values represent the volume of the twin lamellae with respect to its corresponding parent grain. In the case of double twin, the parent grain of the secondary twin is the primary twinned region/grain. Furthermore, volume fractions of the secondary extension twin lamellae are 49% (compression case) and 50% (tension case) of the primary twin volume. Moreover, the primary twin lamella was formed when the value of accumulated twin volume fraction of the predominant twin system reached a threshold value of 1.5% and 1.3% of the central grain volume in the case of simple compression and tension, respectively. Likewise, the second deformation stage generates the secondary predominant twin system of a given volume relative to the volume of the primary twin. After each interruption and each deformation step a transfer of characteristic twin shear between the parent and twin grain is enforced as explained in section 3.3. Next, we explain how these specific primary and secondary twin variants in the central grain were determined along with their corresponding volume fractions.

4.2. Twin variant selection and instantiation

In order to determine which contraction twin system is predominant in the parent grain, we look at the distributions of normalized resolved shear stresses ($\overline{\text{RSSTW}}$) of all 6 available $\{10\bar{1}1\}\langle 10\bar{1}2\rangle$ contraction twin variants after applying the first deformation stage (the pre-strain of 0.073 in simple compression and 0.118 in simple tension). This quantity represents the shear stress resolved on the twin plane and in the twinning direction (RSSTW) that is normalized by its critical value, as entering Eq. (14). Fig. 4 displays the interior of the parent grain (y-z cut) and shows these distributions found across it. Furthermore, it represents a driving force for twin to nucleate, suggesting the spatial region in the parent grain where the twin could initially form. Percent values found below each image show the accumulated twin volume fraction values for the corresponding contraction twin variant. CPFE results show that the $(0\bar{1}11)[0\bar{1}1\bar{2}]$ contraction twin is the predominant twin system in the parent grain.

When forming primary contraction twin lamella, a very important question arises; what is the appropriate place where it would form? Twins occur due to highly localized material behavior, not influenced by the average stress or strain properties. The twin system resolved shear stress is the necessary condition, otherwise the twin variant does not activate. However, many locations over the grain satisfy this criterion as the accumulated twin volume fraction at the strain level of twin formation is finite. Points of the highest stress concentrations in the grain tend to act as favorable twin nucleation sites. These point locations are often, but not necessarily, found at the grain boundaries [84–88]. In our approach as a measure of determining stress concentration points in the model we use Von Mises stress values (Fig. 5b and c, b', and c'). Normalization is performed over the entire volume of the polycrystal with the average value of applied stress. We investigate contours of the normalized RSSTW of the $(0\bar{1}11)[0\bar{1}1\bar{2}]$ contraction twin variant, since this variant, as previously defined, is predominant. Fig. 5 contains plots that were used to identify the exact location where the primary contraction twin lamella (1.5% and 1.3% of the parent volume fraction in compression and tension respectively) was formed. The lower right part of the parent grain was selected as the most favorable location for twin to nucleate, since it is the region of the highest stress concentration and also has the necessary driving force (resolved shear stress) to from the twin (Fig. 5a, b, a', and b').

Furthermore, after performing the second stage of deformation, we found that roughly 50% of the twin volume fraction was accumulated (according to the pseudo-slip model for twinning) on the predominant $(01\bar{1}2)[0\bar{1}11]$ extension twin variant plane within the previously instantiated primary twin volume. Fig. 6 displays contours of $\overline{\text{RSSTW}}$ within the primary twin lamella for all 6 available $\{10\bar{1}2\}\langle 10\bar{1}1\rangle$ extension twin systems. The contours are shown on both sides of the primary contraction twin volume. It shows a tendency of forming an $(01\bar{1}2)[0\bar{1}11]$ extension twin lamella inside the primary twin region. Furthermore, explanation of the double twin classification into different types is provided in the following section.

Finally, Fig. 7 shows views of the granular microstructure and the central grain after each deformation step necessary to form a double twin in simple compression and tension. Once the 50% secondary extension twin lamella was instantiated, the volume of

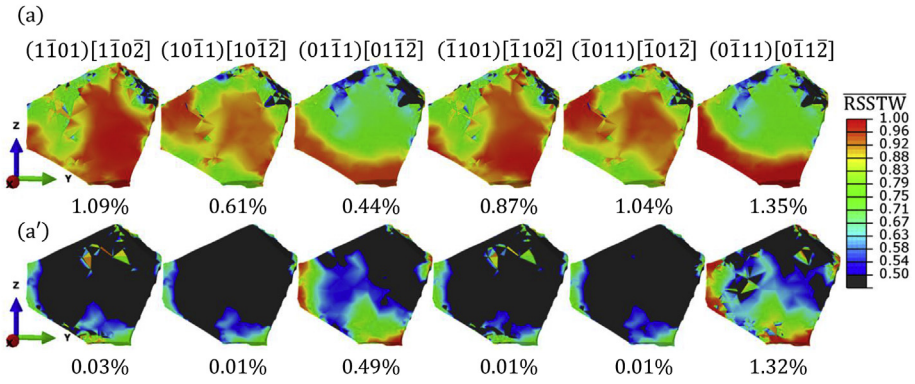

Fig. 4. Distributions of normalized resolved shear stresses along the twin plane and in the twin direction for all six contraction twin variants after a true pre-strain of: (a) 0.073 in simple compression and (a') 0.118 in simple tension, which was necessary to nucleate a primary twin lamella. The normalization was performed with the corresponding critical value for onset of twinning. Percentage values indicated at the bottom represent accumulated twin volume fractions per variant at the given strain levels. The sections are made at x = 0.5, which cuts the parent grain approximately in half.

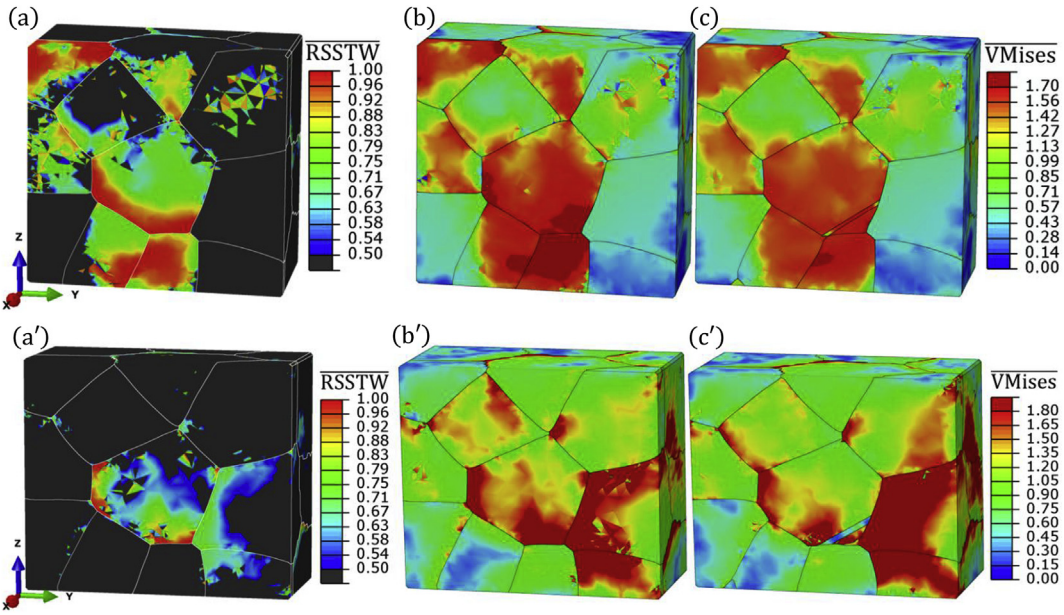

Fig. 5. Distribution of normalized resolved shear stresses ($\overline{\text{RSSTW}}$) for (0$\bar{1}$11)[0$\bar{1}$1$\bar{2}$] predominant contraction twin variant after a pre-strain of (a) 0.073 in simple compression and (a') 0.118 in simple tension. Distributions of von Mises stress normalized by its average value over the granular microstructure: (b) right before and (c) after the formation of 1.5% primary contraction twin lamella in simple compression and (b') right before and (c') after the formation of 1.3% primary contraction twin lamella in simple tension.

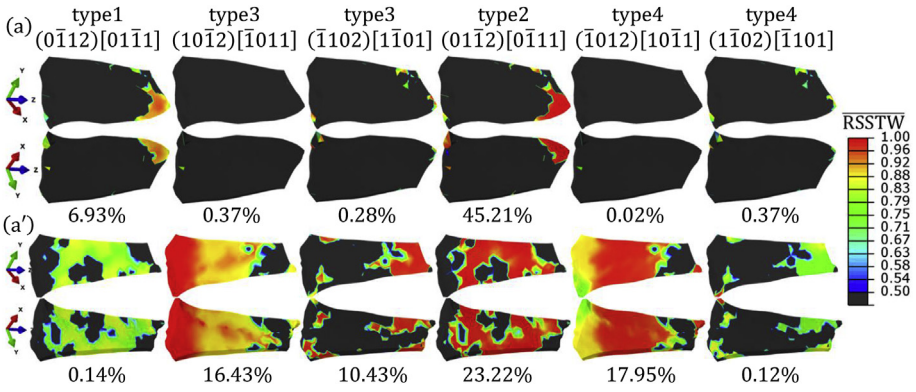

Fig. 6. Distributions of normalized resolved shear stresses within the twin plane (on both sides) and in the twin direction for all six extension variants after the second deformation step to an additional true strain of: (a) 0.056 in simple compression and (a') 0.061 in simple tension, which was imposed to nucleate a secondary twin lamella. The normalization was done with a corresponding critical value of twin resistance values for onset of twinning. Percentage values indicated at the bottom represent accumulated twin volume fractions for each extension twin system at the given strain level.

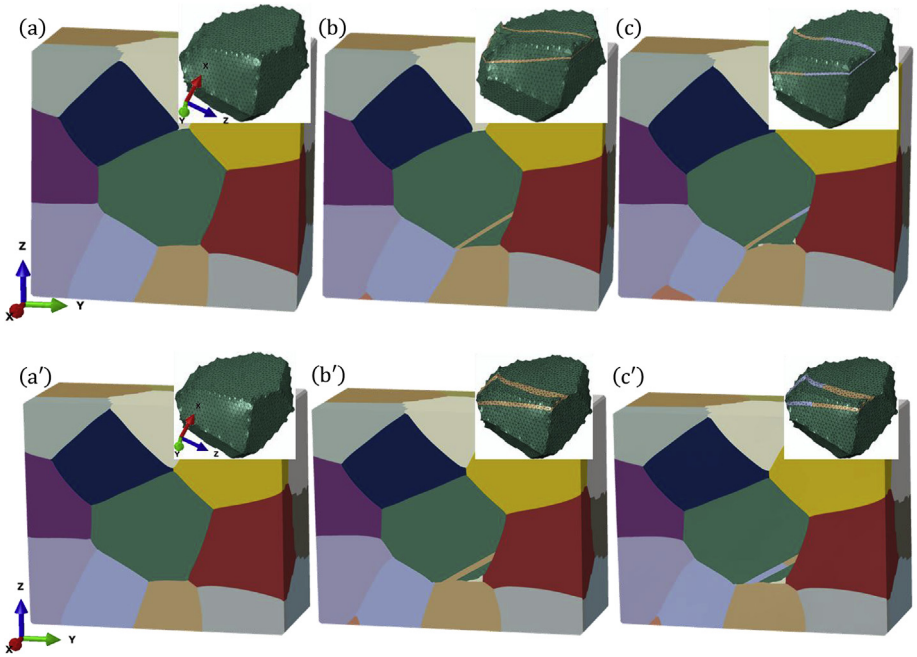

Fig. 7. Double twin formation during simple compression (top row) and simple tension (bottom row) with respect to the surrounding neighboring grains in the 3D granular microstructure. (a and a') Initial microstructure, where the central grain colored in green, is favorably oriented for $\{10\bar{1}1\}\langle 10\bar{1}2\rangle$ contraction twinning. (b and b') Granular microstructure after the formation of the $(0\bar{1}11)[0\bar{1}1\bar{2}]$ primary contraction twin in the parent grain. (c and c') Granular microstructure upon double twin formation, where the secondary extension twin lamella $(01\bar{1}2)[0\bar{1}11]$ is colored in light blue. The unprimed and primed labels are for simple compression and simple tension, respectively. (For interpretation of the references to color in this figure legend, the reader is referred to the Web version of this article.)

the initial primary contraction twin lamella was not changed. This is justified, because in the lateral growth of secondary $\{10\bar{1}2\}$ twins, the final shape of a double twin is mainly enforced by the shape of primary $\{10\bar{1}1\}$ twin [28,29]. However, while the size and the shape of the secondary twin is pre-determined by the size and shape of the primary contraction twin, the primary twin is experiencing a slight distortion due to the secondary twin reorientation and the evolution of local mechanical fields towards a new equilibrium.

4.3. CPFE vs. schmid analysis of primary and secondary twin variants

In general, the material response is highly affected by the rapid reorientation of crystallographic texture due to primary and secondary twinning [36,89,90]. Therefore, an accurate prediction of the most dominant twin variants that occur in the microstructure is of high importance. The most commonly adopted method that has been used to investigate the mechanism of primary and secondary twin variant selection under different loading conditions is Schmid factor analysis [91,92]. Recent statistically significant experimental findings suggest that the behavior of AZ31 Mg alloy deviates from Schmid-like behavior for both primary and secondary twinning [28,53]. This type of behavior usually represents an implication of a locally stress-driven event, when the local stress state in the grain is significantly different from the macroscopically imposed stress state.

A brief background about the two stage twin variant sequence that occurs during the process of double twinning is provided. We focus on the particular double twin variant sequence observed in AZ31 during both simple compression and tension using our 3D CPFE modeling approach which explicitly models double twin lamella. Also provided are the misorientation relations between the original parent (matrix) and doubly twinned volumes.

In terms of twinning in AZ31, we have six contraction and six extension twin variants. In order to form a double twin, each of the six contraction twin variants (cause primary twin reorientation of ~56° around a $\langle 1\bar{2}10\rangle$ axis) can form/nucleate one of the six available extension twin variants (secondary twin reorientation of ~86° around a $\langle 1\bar{2}10\rangle$ axis). Hence, in the most general case double twin formation covers 36 different primary-secondary pairs of twin variants [93]. However, all of them can be classified into only four groups (types) depending on the overall reorientation that they cause with respect to the parent/matrix crystal orientation. Based on our CPFE predictions in both simple compression and tension cases the same double twin variant sequence is predicted. As already stated, the primary predominant contraction twin variant is $(0\bar{1}11)[0\bar{1}1\bar{2}]$, while the secondary predominant extension twin variant is $(01\bar{1}2)[0\bar{1}11]$. More detailed visual representation of the

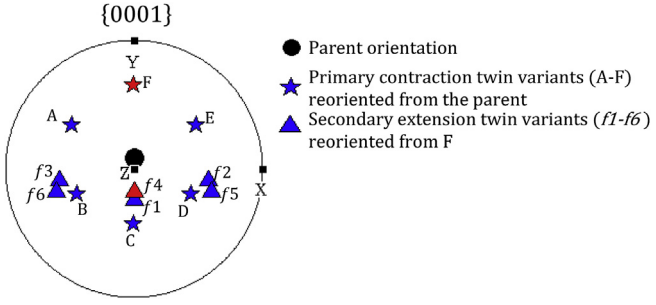

Fig. 8. Stereographic projection of the basal {0001} pole of the initial parent orientation, 6 contraction (primary) and 6 extension (secondary) twin variants. Red colored markers are used to denote the specific twin variants (the predominant twin systems), which are modeled using CPFE as a primary and a secondary twin variant. Secondary extension twin variants (*f1-f6*) reorient from the primary contraction twin variant denoted with red star, F. (For interpretation of the references to color in this figure legend, the reader is referred to the Web version of this article.)

Table 1
Six $\{10\bar{1}1\} - \{10\bar{1}2\}$ double twin variant pairs classified into 4 types. Misorientation angles about the common zone axis between the basal planes of the matrix/parent define the 4 different double twin types.

Double twin variants	$f1$ (type 1)	$f4$ (type 2)	$f2$ and $f3$ (type 3)	$f5$ and $f6$ (type 4)
Misorientation	37.5°	30.1°	66.5°	69.9°

Table 2
Calculated Schmid factor values for basal slip, contraction, and extension twin variants within parent, primary, and secondary twinned regions under simple compression and simple tension. The most heavily stressed twin systems based on the Schmid analysis are tagged with red stars, while those based on the CPFE simulations are tagged with blue stars. The relevant labels of twin variants in the most left column are consistent with those in Table 1 and Fig. 8.

Schmid factor values			Compression			tension		
			parent	primary twin	secondary twin	parent	primary twin	secondary twin
3 basal systems		$(0001)[2\bar{1}\bar{1}0]$	0	0	0	0	0	0
		$(0001)[\bar{1}2\bar{1}0]$	−0.148	0.32	0.279	0.148	−0.32	−0.279
		$(0001)[\bar{1}\bar{1}20]$	0.148	−0.32	−0.279	−0.148	0.32	0.279
6 contraction twin variants	A	$(1\bar{1}01)[1\bar{1}0\bar{2}]$	0.447	−0.122	0.265	0.136	−0.434	−0.047
	B	$(10\bar{1}1)[10\bar{1}\bar{2}]$	0.352	0.083	0.444	0.041	−0.228	0.132
	C	$(01\bar{1}1)[01\bar{1}\bar{2}]$	0.295	−0.075	0.497	0.295	−0.075	0.497
	D	$(\bar{1}101)[\bar{1}10\bar{2}]$	0.352	0.083	0.444	0.041	−0.228	0.132
	E	$(\bar{1}011)[\bar{1}01\bar{2}]$	0.447	−0.122	0.265	0.136	−0.434	−0.047
	F	$(0\bar{1}11)[0\bar{1}1\bar{2}]$	0.486**	−0.486	0.139	0.486**	−0.486	0.139
6 extension twin variants	$f1$	$(0\bar{1}12)[01\bar{1}1]$	−0.458	0.312	−0.403	−0.458	0.312	−0.403
	$f2$	$\left(10\bar{1}2\right)\left[\bar{1}011\right]$	−0.486	0.035	−0.415	−0.112	0.41*	−0.041
	$f3$	$(\bar{1}102)[1\bar{1}01]$	−0.486	0.035	−0.415	−0.112	0.41*	−0.041
	$f4$	$(01\bar{1}2)[0\bar{1}11]$	−0.480	0.361**	−0.361	−0.48	0.361*	−0.361
	$f5$	$(\bar{1}012)[10\bar{1}1]$	−0.475	0.011	−0.436	−0.1	0.385	−0.062
	$f5$	$(1\bar{1}02)[\bar{1}101]$	−0.475	0.011	−0.436	−0.1	0.385	−0.062

above mentioned twin variants is shown in Fig. 8 where red color markers were used to tag these twin variants. Furthermore, Table 1 classifies twin variants into 4 different types, also containing the corresponding misorientation angles from the parent orientation basal plane. According to the table, the selected double twin for the study is classified as type 2. The types 1 and 2 have been observed to frequently form in compression along an axis close to the c-axis [28].

Furthermore, we provide Schmid factor analysis for basal slip systems, contraction and extension twin variant systems under simple compression and tension. We consider crystal orientations in the parent region, as well as in the double twin region. The

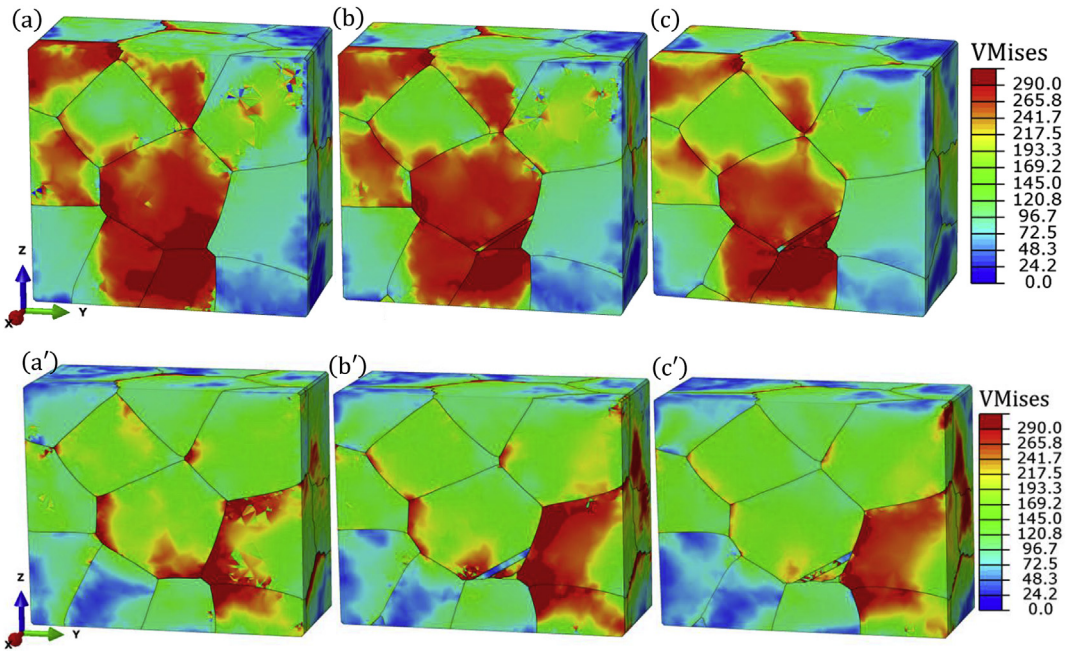

Fig. 9. Distributions of von Mises stress at different stages of double twinning: (a and a') right before $(0\bar{1}11)[0\bar{1}1\bar{2}]$ primary contraction twin formation (end of the first deformation step), (b and b') right before $(01\bar{1}2)[0\bar{1}11]$ secondary extension twin formation (end of the second deformation step), and (c and c') upon double twinning and a small amount of additional deformation of 0.015 true strain (end of the third deformation step). The unprimed and primed labels are for simple compression and simple tension cases, respectively.

results of the analysis are presented in Table 2. Schmid factor of a specific crystallographic system (slip or twin) can be computed as the ratio between the shear stress that can be resolved on the particular slip or twin plane and the macroscopic stress state that is imposed to evaluate the (τ) in the crystal or more conveniently expressed using the angles:

$$M = \tau/\sigma = \cos\lambda \cdot \cos\phi. \quad (17)$$

The angles λ and ϕ represent angles between the loading axis and the crystallographic plane normal and direction vectors, respectively, for each specific crystallographic system. Red stars are put in the table next to the most stressed twin variant systems determined by the analysis. Also, we assume that the macroscopic stress (σ) of unity (1 MPa) was applied for both simple compression and tension cases, to estimate resolved shear stress for each crystal orientation. Due to the directionality of the twinning, twin variants can be activated only if the resolved shear stress (or Schmid factor) is positive.

In compression, results of the Schmid analysis match well with the results obtained from our 3D CPFE modeling approach. In fact, the most heavily stressed twin systems (highest Schmid factor-marked with a red star in Table 2) are found to be the most dominant ones in the CPFE simulations (marked with a blue star in Table 2). However, in the tension case, twin variant selection slightly deviates from the Schmid-like behavior, because the secondary predominant extension twin variant system does not have the highest Schmid factor value. The Schmid analysis predicts the rarely observed type 3 sequence. An interesting observation which we find important to note here is that in simple tension all 6 available extension twin variants possess relatively high and similar Schmid factor values.

5. Stress fields as predicted by CPFE

Fig. 9 shows the evolution of von Mises stress fields across the granular microstructure as the double twin forms during simple compression and tension deformation steps. The material parameters used in the dislocation density hardening law were calibrated for AZ31 to capture its material response across a large range of different strain rates and temperatures [77]. Hence, the stress magnitude shown are realistic and are not normalized. As more strain is applied, double twin forms in the parent grain interior, which is followed by the increase in stress magnitude in the vicinity of the formed double twin. It is noticeable that this event affects the stress distribution in some of the neighboring grains as well. These specific details are governed by the particular grain orientations, morphology of the grain boundary surfaces, and history of loading.

Furthermore, we investigate how plastic strain is accommodated across the granular microstructure as external deformation is applied. Fig. 10 shows strain concentration distributions ($\overline{\text{PEEQ}}$ -

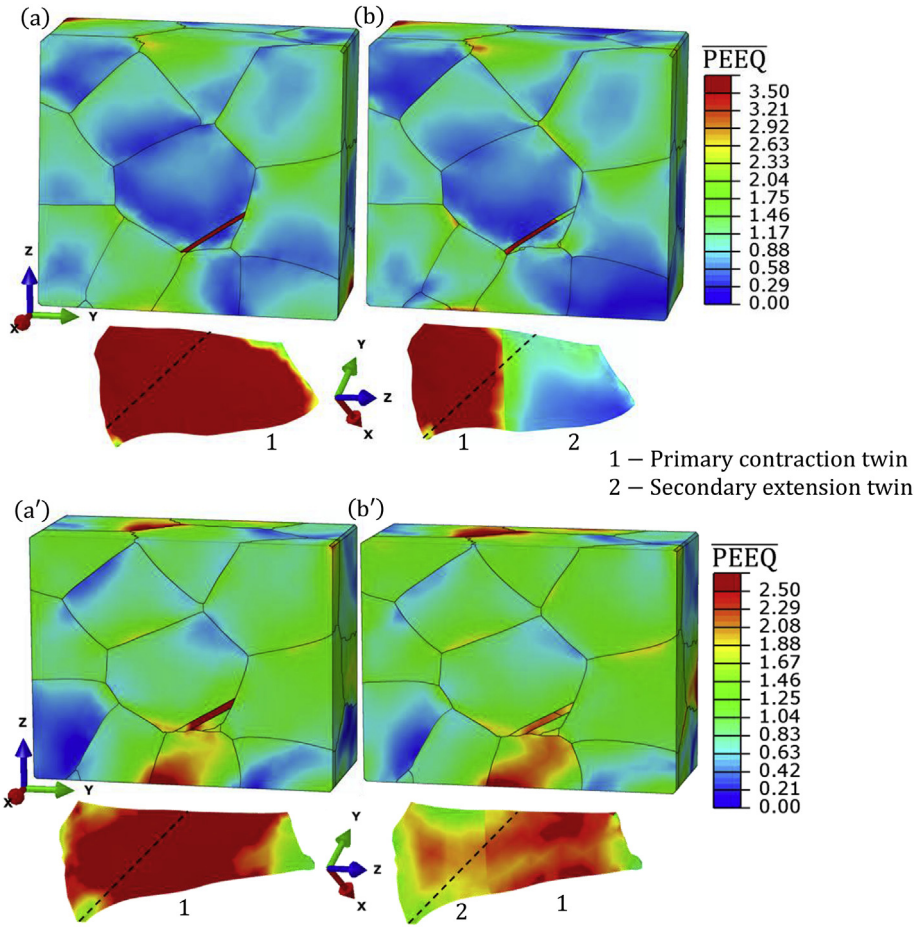

Fig. 10. Distributions of normalized value of equivalent plastic strain ($\overline{\text{PEEQ}}$) (a) right before and (b) after secondary twin formation in simple compression and (a') right before and (b') after secondary twin formation in simple tension. Note that in (b) and (b') a small amount of additional deformation of 0.015 true strain was applied upon double twinning. The inserts show the contours across primary contraction and secondary extension portions of the double twin. Dashed lines superimposed over the inserts show the location of the planes used to cut the upper granular microstructures. The normalization is performed by the applied equivalent plastic strain value.

equivalent plastic strain is normalized with the applied strain) after primary and secondary twin lamellae have been introduced. The plots shown correspond to the deformation states after the second and third deformation stages in simple compression and tension. An interesting conclusion can be drawn that most of the strain is contained in the primary contraction twin lamella region. This state remains even after secondary twin lamella is formed. Fig. 11 can explain this kind of behavior by providing the distributions of the accumulated shear strains for basal and prismatic slip modes for the corresponding deformation steps. These values are plotted at the end of each performed deformation stage ensuring the same strain levels. These slip activity maps show the amount of basal and prismatic shear strains accumulated in each of the three deformation steps that were carried out for the corresponding externally applied strain increments. Hence, for each deformation step these values start from zero and accumulate as the external deformation is applied. The double twin region is favorable for basal slip due to the twin induced crystal reorientation. Moreover, the basal slip mode has the highest activity within the primary contraction twin lamella. As a result, the strain energy is predicted to be lower upon twin instantiation.

In order to better understand the inhomogeneity introduced by formation of double twin, we examine distributions of traction forces at the double twin-parent boundary. This boundary is initially introduced by the formation of the primary contraction twin lamella and, subsequently modified by secondary twinning to consist of two crystallographically different parts, where parent and either contraction or extension twin meet. Fig. 12 shows the

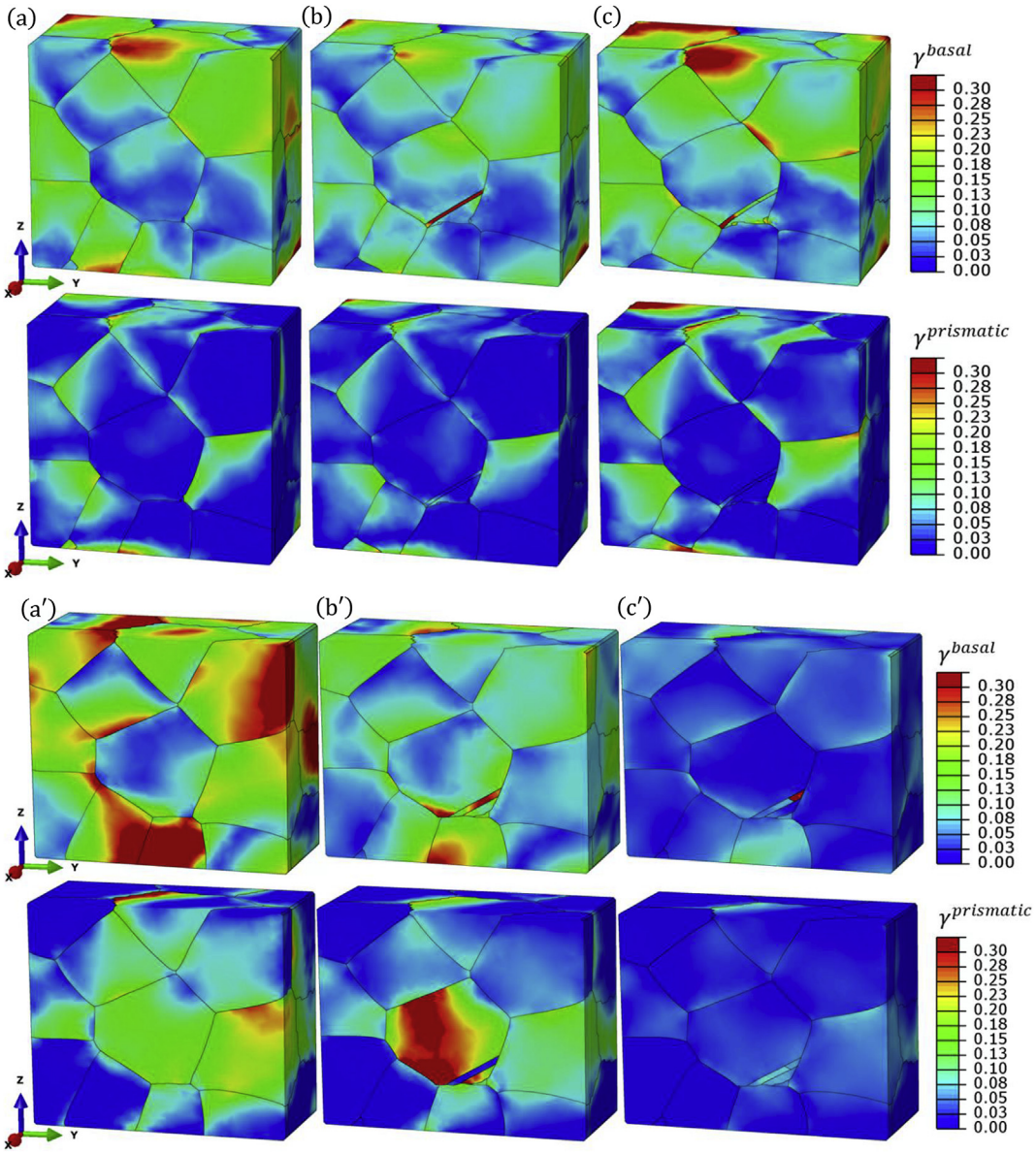

Fig. 11. Distributions of the accumulated shear strains across the whole grain model for basal and prismatic slip modes: (a and a') right before primary contraction twin formation (end of the first deformation step), (b and b') right before secondary extension twin formation (end of the second deformation step), and (c and c') upon double twinning and a small amount of additional deformation of 0.015 true strain (end of the third deformation step). The unprimed and primed labels correspond to simple compression and simple tension cases, respectively. Note that the values are initialized before a given deformation step and refect those accumulated during the given deformation step. The model was consecutively deformed in true strain increments of 0.073, 0.056 and 0.015 for the compression case, while those for the tension case are 0.118, 0.061 and 0.015. Note that the model was much less deformed in the third deformation stage relative to the first two stages. As a result, the basal and prismatic shear strains have lower values in the third stage.

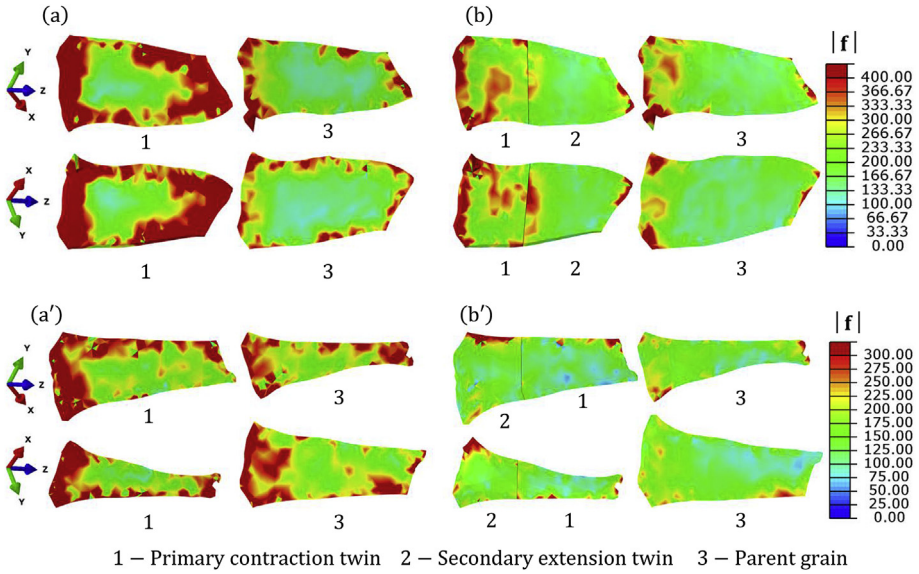

Fig. 12. Distributions of magnitude of traction force across the twin-parent boundary: (a and a') right before secondary extension twin formation (end of the second deformation step) and (b and b') upon double twinning and a small amount of additional deformation of 0.015 true strain (end of the third deformation step). Both sides of the twin-parent boundaries are shown. The unprimed and primed labels are for simple compression and simple tension, respectivelly.

distributions of traction force magnitude that are spatially resolved across twin-matrix boundaries at the end of the second and the third deformation steps in simple compression and tension. Both sides of the double twin-parent boundary are shown (i.e. from twin's and parent's side). The field on the parent side is calculated from stress in the finite element layer of the parent adjacent to the interface ($\boldsymbol{\sigma}^{parent}$), while the field on the twin size is calculated from stress in the element layer in the twin adjacent to the interface ($\boldsymbol{\sigma}^{tw}$). The traction force vector is obtained as a projection of the Cauchy stress tensor in each finite element on the twin lamella normal and its magnitude is calculated using: $|\mathbf{f}| = |\boldsymbol{\sigma}\cdot\mathbf{v}^{tw,pts}|$, as schematically shown in Fig. 13. Note that the vector $\mathbf{v}^{tw,pts}$ is conveniently defined to locally change its direction over the interface as it always points from the twin to the parent, unlike the crystallographic plane normal $\mathbf{n}^{tw,pts}$. Existence of the spatial gradient in the magnitude of the traction force across and over the interface indicates that fracture could initiate from the twin-matrix interface.

The magnitude of the traction force shown in Fig. 12 does not convey the maximum acting direction. Fig. 14 shows the difference in traction force at the twin-parent interface (i.e. between the parent and the twin side of the interface) in the direction pointing from the twinned region towards the parent surrounding (Fig. 13). It is computed using the relationship:

$$\Delta f = \mathbf{f}^{parent}\cdot\mathbf{v}^{tw,pts} - \mathbf{f}^{twin}\cdot\mathbf{v}^{tw,pts}$$

The difference between traction forces in this particular direction, $\mathbf{v}^{tw,pts}$, further confirms the heterogeneity in the field created by double twinning that can lead to void initiation and propagation to failure. Variation in the tensile and compressive sense of the traction forces along the $\mathbf{v}^{tw,pts}$ direction is the highest along the primary contraction twin-parent boundary for both simple compression and tension cases. In particular, the predicted tensile traction region points to void formation from the twinned region, as experimentally observed in Ref. [10]. The voids were observed to extend along a significant portion of the twinned region or sometimes even to form in the twin interior. In summary, the presence of a strong traction force gradient of even variable sign suggests that twin-parent interface is a favorable void nucleation site in the microstructure. Future work will consider the implementation of cohesive zone elements at the twin-parent interface to facilitate modeling of interface decohesion.

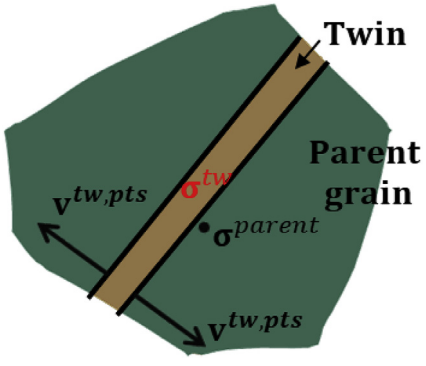

Fig. 13. Schematic of the twin-matrix boundaries showing the vector $\mathbf{v}^{tw,pts}$ pointing from twinned region to its surrounding.

6. Summary and conclusions

In this work, a recently developed CPFE framework for explicit modeling of microstructure is extended to model a discrete double twin lamella. The present study is applied to a magnesium alloy AZ31, an HCP material that deforms by a combination of crystallographic slip and deformation twinning, and has a tendency of forming double twins. These twins are experimentally found to lead to a void formation and failure of AZ31. A polycrystal in the form of synthetically generated granular microstructure was studied in simple compression and tension. A centrally located grain in the microstructure surrounded by the largest number of neighboring grains was chosen to form a double twin lamella. The lamella was developed by executing three consecutive deformation stages consisting of pre-straining (to form a primary contraction twin), followed by straining (to form a secondary extension twin), and finally a small amount of additional deformation upon double

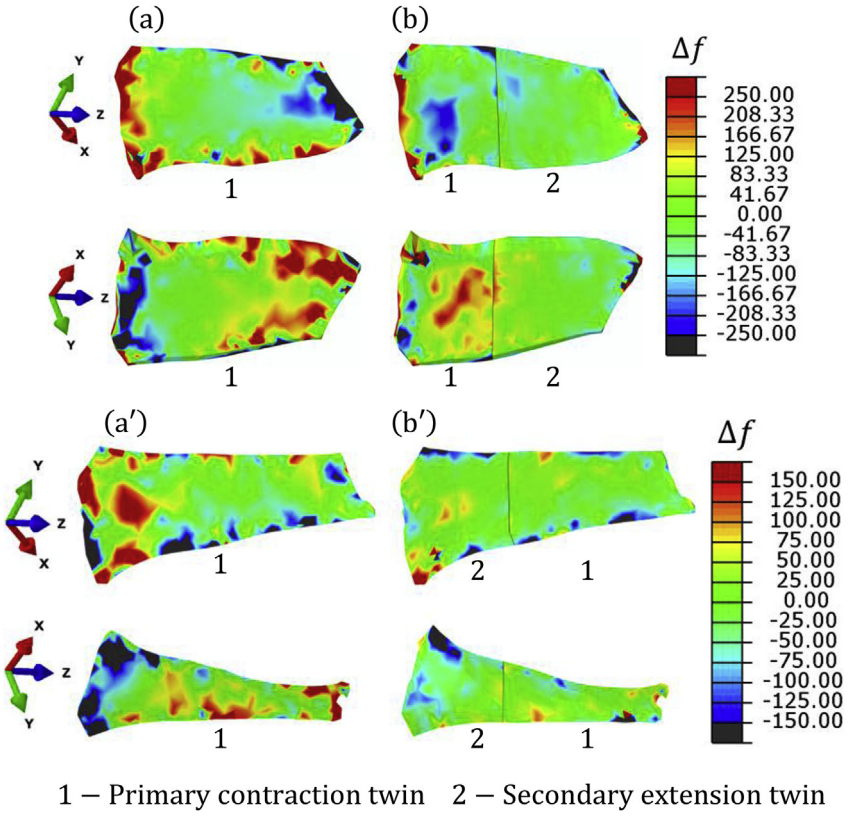

Fig. 14. Distributions of the difference in the projected traction force along **v** between parent grain and twinned region at the twin-parent interface: (a and a') right before secondary extension twin formation (end of the second deformation step) and (b and b') upon double twinning and a small amount of additional deformation of 0.015 true strain (end of the third deformation step). The unprimed and primed labels are for simple compression and simple tension, respectivelly.

twinning. While all constituent grains in the microstructure were allowed to deform by slip and twinning, the explicit modeling of a twin lamella was performed only for the suitably oriented central grain. The model successfully predicts the most commonly observed "double twin" sequence, $(0\bar{1}11)[0\bar{1}1\bar{2}] - (01\bar{1}2)[0\bar{1}11]$, as the most likely to occur in both simple compression and simple tension. The predicted sequence in the parent grain obtained using the CPFE simulations in simple compression match well with the corresponding results of the Schmid analysis. In contrast, in the tension case, the twin variant selection based on CPFE deviated from the one based on the Schmid analysis. The stress fields predicted by CPFE govern the correct sequence. Furthermore, the predicted stress fields in the microstructure with the double twin reveals a greater strain concentration in the close vicinity of the initially formed primary contraction twin than in the secondary twin. The primary contraction twin region was predicted to deform by a large amount of basal slip. Finally, the investigation of the traction forces acting on a double twin-parent interface reveals that the contraction twin-parent interface is a weak link in the microstructural grain boundary network, which is susceptible to void nucleation.

Acknowledgements

This work is based upon a project supported by the U.S. National Science Foundation (NSF) under grant no. CMMI-1650641. M. A. also wishes to acknowledge the support from the graduate school at the University of New Hampshire through the Dissertation Year Fellowship program.

Appendix A

For completeness of the presented constitutive model, we provide a summary of the utilized dislocation density hardening law. This formulation of the hardening law was used to compute the evolution of slip and twin resistances as a function of strain, temperature, and strain rate [65,83].

In order to estimate the resistance required to trigger slip, we take into account the contributions of the following terms: a friction stress $\tau^{\alpha}_{0,f}$, a forest dislocation interaction stress τ^{α}_{for} and a dislocation substructure interaction stress τ^{α}_{sub}:

$$\tau^{\alpha}_{c} = \tau^{\alpha}_{0,f} + \tau^{\alpha}_{for} + \tau^{\alpha}_{sub}. \tag{A1}$$

The resistance for twin activation evolves considering a temperature-independent friction term τ^{β}_{0} and a latent hardening term which performs coupling between the active slip and twin systems. Accounting for both effects, the resistance for twinning is expressed as:

$$\tau^{\beta}_{c} = \tau^{\beta}_{0} + \mu^{\beta}\sum_{\alpha} C^{\alpha\beta} b^{\beta} b^{\alpha} \rho^{\alpha}_{for}. \tag{A2}$$

In this relationship μ^{β}, b^{β} and $C^{\alpha\beta}$ represent respectively the elastic shear modulus, Burgers vector on the given twin system, and the latent hardening matrix used for coupling. Furthermore, the individual behavior of τ^{α}_{for} and τ^{α}_{sub} is determined by the evolution of the dislocation densities that consist of forest ρ^{α}_{for} and substructure ρ^{α}_{sub} dislocations. For this purpose a Taylor-like law is used to represent these relationships for each dislocation type. These are expressed as:

$$\tau_{for}^{\alpha} = \chi b^{\alpha}\mu^{\alpha}\sqrt{\rho_{for}^{\alpha}}, \tag{A3}$$

$$\tau_{sub}^{\alpha} = k_{sub}\mu^{\alpha}b^{\alpha}\sqrt{\rho_{sub}}log\left(\frac{1}{b^{\alpha}\sqrt{\rho_{sub}}}\right). \tag{A4}$$

Here χ is a dislocation interaction parameter set to 0.9 and $k_{sub} = 0.086$ is a mathematical parameter that insures that Eq. (A3) compensates the Taylor law at low dislocation densities [94]. The initial material state corresponds to an annealed state, hence the initial dislocation density was set to $10^{12}\,m^{-2}$. The value of stored forest density ρ_{for}^{α} changes according to competition between the rate of storage/generation and the rate of dynamic recovery/removal:

$$\frac{\partial\rho_{for}^{\alpha}}{\partial\gamma^{\alpha}} = \frac{\partial\rho_{gen,for}^{\alpha}}{\partial\gamma^{\alpha}} - \frac{\partial\rho_{rem,for}^{\alpha}}{\partial\gamma^{\alpha}} = k_1^{\alpha}\sqrt{\rho_{for}^{\alpha}} - k_2^{\alpha}(\dot{\varepsilon},T)\rho_{for}^{\alpha}, \quad \Delta\rho_{for}^{\alpha} = \frac{\partial\rho_{for}^{\alpha}}{\partial\gamma^{\alpha}}|\Delta\gamma^{\alpha}|. \tag{A5}$$

In Eq. (A5) k_1^{α} is a coefficient for the rate of dislocation storage because of statistical trapping of gliding dislocations and k_2^{α} is the coefficient for the rate of dynamic recovery by thermally activated mechanisms. The second coefficient can be determined by this relationship:

$$\frac{k_2^{\alpha}(\dot{\varepsilon},T)}{k_1^{\alpha}} = \frac{\chi b^{\alpha}}{g^{\alpha}}\left(1 - \frac{kT}{D^{\alpha}b^3}ln\left(\frac{\dot{\varepsilon}}{\dot{\varepsilon}_0}\right)\right), \tag{A6}$$

where k, $\dot{\varepsilon}_0$, g^{α} and D^{α} are respectively Boltzmann's constant, a reference strain rate (taken here to be $10^7\ s^{-1}$), an effective activation enthalpy and a drag stress. Lastly, the increment in substructure development can be related to the rate of dynamic recovery of all active dislocations as:

$$\Delta\rho_{sub} = \sum_{\alpha} qb^{\alpha}\frac{\partial\rho_{rem,for}^{\alpha}}{\partial\gamma^{\alpha}}|\Delta\gamma^{\alpha}|, \tag{A7}$$

where q is a rate parameter that determines the fraction of an α -type dislocations that do not annihilate, but become substructure dislocation. As previously mentioned in the text, the material parameters used in this hardening law have been calibrated in a prior study.

References

[1] M. Ardeljan, R.J. McCabe, I.J. Beyerlein, M. Knezevic, Explicit incorporation of deformation twins into crystal plasticity finite element models, Comput. Meth. Appl. Mech. Eng. 295 (2015) 396–413.
[2] K. Cho, T. Sano, K. Doherty, C. Yen, G. Gazonas, J. Montgomery, P. Moy, B. Davis, R. DeLorme, Magnesium Technology and Manufacturing for Ultra Lightweight Armored Ground Vehicles, DTIC Document, 2009.
[3] B.L. Mordike, T. Ebert, Magnesium: properties - applications - potential, Mater. Sci. Eng. 302 (2001) 37–45.
[4] M.M. Avedesian, H. Baker, Magnesium and Magnesium Alloys - ASM Speciality Handbook, ASM International, Materials Park, Ohio, 1999.
[5] W. Hosford, T. Allen, Twinning and directional slip as a cause for a strength differential effect, Metall. Mater. Trans. B 4 (1973) 1424–1425.
[6] E.F. Horst, B. Mordike, Magnesium Technology. Metallurgy, Design Data, Application, Springer-Verlag, Berlin Heidelberg, Germany, 2006.
[7] W.F. Hosford, Mechanical Behavior of Materials, Cambridge University Press, New York, NY, USA, 2010.
[8] X.Y. Lou, M. Li, R.K. Boger, S.R. Agnew, R.H. Wagoner, Hardening evolution of AZ31B Mg sheet, Int. J. Plast. 23 (2007) 44–86.
[9] T. Al-Samman, G. Gottstein, Room temperature formability of a magnesium AZ31 alloy: examining the role of texture on the deformation mechanisms, Mater. Sci. Eng. 488 (2008) 406–414.
[10] M.R. Barnett, Twinning and the ductility of magnesium alloys: Part II. "Contraction" twins, Mater. Sci. Eng. 464 (2007) 8–16.
[11] A. Jain, O. Duygulu, D.W. Brown, C.N. Tomé, S.R. Agnew, Grain size effects on the tensile properties and deformation mechanisms of a magnesium alloy, AZ31B, sheet, Mater. Sci. Eng. 486 (2008) 545–555.
[12] M. Lentz, A. Behringer, C. Fahrenson, I.J. Beyerlein, W. Reimers, Grain size effects on primary, secondary, and tertiary twin development in Mg-4 wt pct Li (-1 wt pct Al) alloys, Metall. Mater. Trans. 45 (2014) 4737–4741.
[13] M. Jahedi, B.A. McWilliams, P. Moy, M. Knezevic, Deformation twinning in rolled WE43-T5 rare earth magnesium alloy: influence on strain hardening and texture evolution, Acta Mater. 131 (2017) 221–232.
[14] M. Lentz, M. Klaus, M. Wagner, C. Fahrenson, I.J. Beyerlein, M. Zecevic, W. Reimers, M. Knezevic, Effect of age hardening on the deformation behavior of an Mg–Y–Nd alloy: in-situ X-ray diffraction and crystal plasticity modeling, Mater. Sci. Eng. 628 (2015) 396–409.
[15] M. Jahedi, B.A. McWilliams, F.R. Kellogg, I.J. Beyerlein, M. Knezevic, Rate and temperature dependent deformation behavior of as-cast WE43 magnesium-rare earth alloy manufactured by direct-chill casting, Mater. Sci. Eng. 712 (2018) 50–64.
[16] M. Jahedi, B.A. McWilliams, M. Knezevic, Deformation and fracture mechanisms in WE43 magnesium-rare earth alloy fabricated by direct-chill casting and rolling, Mater. Sci. Eng. 726 (2018) 194–207.
[17] A. Akhtar, E. Teghtsoonian, Solid solution strengthening of magnesium single crystals—I alloying behaviour in basal slip, Acta Metall. 17 (1969) 1339–1349.
[18] C.S. Roberts, Magnesium and its Alloys, Wiley, New York/London, 1960.
[19] T. Obara, H. Yoshinga, S. Morozumi, 11-22<-1-123> Slip system in magnesium, Acta Metall. 21 (1973) 845–853.
[20] D. Nugmanov, M. Knezevic, M. Zecevic, O. Sitdikov, M. Markushev, I.J. Beyerlein, Origin of plastic anisotropy in (ultra)-fine-grained Mg–Zn–Zr alloy processed by isothermal multi-step forging and rolling: experiments and modeling, Mater. Sci. Eng. 713 (2018) 81–93.
[21] H. Yoshinaga, T. Obara, S. Morozumi, Twinning deformation in magnesium compressed along the C-axis, Mater. Sci. Eng. 12 (1973) 255–264.
[22] P.G. Partridge, The crystallography and deformation modes of hexagonal close-packed metals, Metallurgia Revised 12 (1967) 169.
[23] M.H. Yoo, Slip, twinning, and fracture in hexagonal close-packed metals, Metall. Mater. Trans. 12 (1981) 409–418.
[24] J.W. Christian, S. Mahajan, Deformation twinning, Prog. Mater. Sci. 39 (1995), 1–157.
[25] C.S. Barrett, Structure of Metals, McGraw-Hill Book Company, Inc., New York, 1952.
[26] M. Knezevic, A. Levinson, R. Harris, R.K. Mishra, R.D. Doherty, S.R. Kalidindi, Deformation twinning in AZ31: influence on strain hardening and texture evolution, Acta Mater. 58 (2010) 6230–6242.
[27] L. Jiang, J.J. Jonas, R.K. Mishra, A.A. Luo, A.K. Sachdev, S. Godet, Twinning and texture development in two Mg alloys subjected to loading along three different strain paths, Acta Mater. 55 (2007) 3889.
[28] M.R. Barnett, Z. Keshavarz, A.G. Beer, X. Ma, Non-Schmid behaviour during secondary twinning in a polycrystalline magnesium alloy, Acta Mater. 56 (2008) 5–15.
[29] P. Cizek, M.R. Barnett, Characteristics of the contraction twins formed close to the fracture surface in Mg-3Al-1Zn alloy deformed in tension, Scripta Mater. 59 (2008) 959–962.
[30] I. Beyerlein, J. Wang, M. Barnett, C. Tomé, Double twinning mechanisms in magnesium alloys via dissociation of lattice dislocations, Proc. Roy. Soc. Lond. Math. Phys. Sci. 468 (2012) 1496–1520.
[31] B.C. Wonsiewicz, W.A. Backofen, Plasticity of magnesium crystals, Trans. Metall. Soc. AIME 239 (1967).
[32] R. Reed-Hill, W. Robertson, Additional modes of deformation twinning in magnesium, Acta Metall. 5 (1957) 717–727.
[33] D. Ando, J. Koike, Y. Sutou, The role of deformation twinning in the fracture behavior and mechanism of basal textured magnesium alloys, Mater. Sci. Eng. 600 (2014) 145–152.
[34] J. Koike, N. Fujiyama, D. Ando, Y. Sutou, Roles of deformation twinning and dislocation slip in the fatigue failure mechanism of AZ31 Mg alloys, Scripta Mater. 63 (2010) 747–750.
[35] M. Lentz, M. Risse, N. Schaefer, W. Reimers, I.J. Beyerlein, Strength and ductility with {1011} — {1012} double twinning in a magnesium alloy, Nat. Commun. 7 (2016) 11068.
[36] S. Niknejad, S. Esmaeili, N.Y. Zhou, The role of double twinning on transgranular fracture in magnesium AZ61 in a localized stress field, Acta Mater. 102 (2016) 1–16.
[37] M. Knezevic, R.A. Lebensohn, O. Cazacu, B. Revil-Baudard, G. Proust, S.C. Vogel, M.E. Nixon, Modeling bending of α-titanium with embedded polycrystal plasticity in implicit finite elements, Mater. Sci. Eng. 564 (2013) 116–126.
[38] M. Knezevic, M. Zecevic, I.J. Beyerlein, J.F. Bingert, R.J. McCabe, Strain rate and temperature effects on the selection of primary and secondary slip and twinning systems in HCP Zr, Acta Mater. 88 (2015) 55–73.
[39] T.R. Bieler, L. Wang, A.J. Beaudoin, P. Kenesei, U. Lienert, In situ characterization of twin nucleation in pure Ti using 3D-XRD, Metall. Mater. Trans. 45 (2014) 109–122.
[40] B. Morrow, R. McCabe, E. Cerreta, C. Tomé, In-Situ TEM observation of twinning and detwinning during cyclic loading in Mg, Metall. Mater. Trans. 45 (2014) 36–40.
[41] M. Zecevic, M. Knezevic, I.J. Beyerlein, C.N. Tomé, An elasto-plastic self-consistent model with hardening based on dislocation density, twinning and

de-twinning: application to strain path changes in HCP metals, Mater. Sci. Eng. 638 (2015) 262–274.
[42] M. Knezevic, I.J. Beyerlein, D.W. Brown, T.A. Sisneros, C.N. Tomé, A polycrystal plasticity model for predicting mechanical response and texture evolution during strain-path changes: application to beryllium, Int. J. Plast. 49 (2013) 185–198.
[43] G.I. Taylor, Plastic strain in metals, J. Inst. Met. 62 (1938) 307–324.
[44] M. Knezevic, S.R. Kalidindi, D. Fullwood, Computationally efficient database and spectral interpolation for fully plastic Taylor-type crystal plasticity calculations of face-centered cubic polycrystals, Int. J. Plast. 24 (2008) 1264–1276.
[45] M. Knezevic, D.J. Savage, A high-performance computational framework for fast crystal plasticity simulations, Comput. Mater. Sci. 83 (2014) 101–106.
[46] M. Knezevic, S.R. Kalidindi, R.K. Mishra, Delineation of first-order closures for plastic properties requiring explicit consideration of strain hardening and crystallographic texture evolution, Int. J. Plast. 24 (2008) 327–342.
[47] R.A. Lebensohn, C.N. Tomé, A self-consistent anisotropic approach for the simulation of plastic deformation and texture development of polycrystals: application to zirconium alloys, Acta Metall. Mater. 41 (1993) 2611–2624.
[48] R.A. Lebensohn, M. Zecevic, M. Knezevic, R.J. McCabe, Average intragranular misorientation trends in polycrystalline materials predicted by a viscoplastic self-consistent approach, Acta Mater. 104 (2016) 228–236.
[49] M. Zecevic, W. Pantleon, R.A. Lebensohn, R.J. McCabe, M. Knezevic, Predicting intragranular misorientation distributions in polycrystalline metals using the viscoplastic self-consistent formulation, Acta Mater. 140 (2017) 398–410.
[50] J.S. Carpenter, T. Nizolek, R.J. McCabe, M. Knezevic, S.J. Zheng, B.P. Eftink, J.E. Scott, S.C. Vogel, T.M. Pollock, N.A. Mara, I.J. Beyerlein, Bulk texture evolution of nanolamellar Zr–Nb composites processed via accumulative roll bonding, Acta Mater. 92 (2015) 97–108.
[51] H. Abdolvand, M. Majkut, J. Oddershede, J.P. Wright, M.R. Daymond, Study of 3-D stress development in parent and twin pairs of a hexagonal close-packed polycrystal: Part I – in-situ three-dimensional synchrotron X-ray diffraction measurement, Acta Mater. 93 (2015) 246–255.
[52] C. Aydıner, J. Bernier, B. Clausen, U. Lienert, C. Tomé, D. Brown, Evolution of stress in individual grains and twins in a magnesium alloy aggregate, Phys. Rev. B 80 (2009) 024113.
[53] H. Abdolvand, M. Majkut, J. Oddershede, S. Schmidt, U. Lienert, B.J. Diak, P.J. Withers, M.R. Daymond, On the deformation twinning of Mg AZ31B: a three-dimensional synchrotron X-ray diffraction experiment and crystal plasticity finite element model, Int. J. Plast. 70 (2015) 77–97.
[54] L. Balogh, S. Niezgoda, A. Kanjarla, D. Brown, B. Clausen, W. Liu, C. Tomé, Spatially resolved in situ strain measurements from an interior twinned grain in bulk polycrystalline AZ31 alloy, Acta Mater. 61 (2013) 3612–3620.
[55] R.Y. Zhang, M.R. Daymond, R.A. Holt, A finite element model of deformation twinning in zirconium, Mater. Sci. Eng. 473 (2008) 139–146.
[56] M.R. Barnett, N. Stanford, A. Ghaderi, F. Siska, Plastic relaxation of the internal stress induced by twinning, Acta Mater. 61 (2013) 7859–7867.
[57] A.M. Kumar, A.K. Kanjarla, S.R. Niezgoda, R.A. Lebensohn, C.N. Tomé, Numerical study of the stress state of a deformation twin in magnesium, Acta Mater. 84 (2015) 349–358.
[58] J. Cheng, S. Ghosh, Crystal plasticity finite element modeling of discrete twin evolution in polycrystalline magnesium, J. Mech. Phys. Solid. 99 (2017) 512–538.
[59] M. Ardeljan, M. Knezevic, T. Nizolek, I.J. Beyerlein, N.A. Mara, T.M. Pollock, A study of microstructure-driven strain localizations in two-phase polycrystalline HCP/BCC composites using a multi-scale model, Int. J. Plast. 74 (2015) 35–57.
[60] M. Ardeljan, I.J. Beyerlein, M. Knezevic, A dislocation density based crystal plasticity finite element model: application to a two-phase polycrystalline HCP/BCC composites, J. Mech. Phys. Solid. 66 (2014) 16–31.
[61] J. Cheng, J. Shen, R.K. Mishra, S. Ghosh, Discrete twin evolution in Mg alloys using a novel crystal plasticity finite element model, Acta Mater. 149 (2018) 142–153.
[62] M. Ardeljan, M. Knezevic, M. Jain, S. Pathak, A. Kumar, N. Li, N.A. Mara, J.K. Baldwin, I.J. Beyerlein, Room temperature deformation mechanisms of Mg/Nb nanolayered composites, J. Mater. Res. 33 (2018) 1311–1332.
[63] M. Knezevic, I.J. Beyerlein, Multiscale modeling of microstructure-property relationships of polycrystalline metals during thermo-mechanical deformation, Adv. Eng. Mater. 20 (2018) 1700956.
[64] M. Knezevic, M.R. Daymond, I.J. Beyerlein, Modeling discrete twin lamellae in a microstructural framework, Scripta Mater. 121 (2016) 84–88.
[65] I.J. Beyerlein, C.N. Tomé, A dislocation-based constitutive law for pure Zr including temperature effects, Int. J. Plast. 24 (2008) 867–895.
[66] P. Van Houtte, Simulation of the rolling and shear texture of brass by the Taylor theory adapted for mechanical twinning, Acta Metall. Mater. 26 (1978) 591–604.
[67] S.R. Kalidindi, Incorporation of deformation twinning in crystal plasticity models, J. Mech. Phys. Solid. 46 (1998) 267–271.
[68] M. Knezevic, M. Zecevic, I.J. Beyerlein, R.A. Lebensohn, A numerical procedure enabling accurate descriptions of strain rate-sensitive flow of polycrystals within crystal visco-plasticity theory, Comput. Meth. Appl. Mech. Eng. 308 (2016) 468–482.
[69] K.-J. Bathe, Finite Element Procedures, Prentice Hall, Englewood Cliffs, N.J, 1996.
[70] M. Zecevic, R.J. McCabe, M. Knezevic, A new implementation of the spectral crystal plasticity framework in implicit finite elements, Mech. Mater. 84 (2015) 114–126.
[71] M. Zecevic, I.J. Beyerlein, M. Knezevic, Coupling elasto-plastic self-consistent crystal plasticity and implicit finite elements: applications to compression, cyclic tension-compression, and bending to large strains, Int. J. Plast. 93 (2017) 187–211.
[72] S.R. Kalidindi, C.A. Bronkhorst, L. Anand, Crystallographic texture evolution in bulk deformation processing of FCC metals, J. Mech. Phys. Solid. 40 (1992) 537–569.
[73] S.R. Kalidindi, H.K. Duvvuru, M. Knezevic, Spectral calibration of crystal plasticity models, Acta Mater. 54 (2006) 1795–1804.
[74] M. Ardeljan, D.J. Savage, A. Kumar, I.J. Beyerlein, M. Knezevic, The plasticity of highly oriented nano-layered Zr/Nb composites, Acta Mater. 115 (2016) 189–203.
[75] R.J. Asaro, A. Needleman, Texture development and strain hardening in rate dependent polycrystals, Acta Metall. Mater. 33 (1985) 923–953.
[76] J.W. Hutchinson, Bounds and self-consistent estimates for creep of polycrystalline materials, Proc. Roy. Soc. Lond. Math. Phys. Sci. 348 (1976) 101–126.
[77] M. Ardeljan, I.J. Beyerlein, B.A. McWilliams, M. Knezevic, Strain rate and temperature sensitive multi-level crystal plasticity model for large plastic deformation behavior: application to AZ31 magnesium alloy, Int. J. Plast. 83 (2016) 90–109.
[78] M. Knezevic, L. Capolungo, C.N. Tomé, R.A. Lebensohn, D.J. Alexander, B. Mihaila, R.J. McCabe, Anisotropic stress-strain response and microstructure evolution of textured α-uranium, Acta Mater. 60 (2012) 702–715.
[79] M. Groeber, S. Ghosh, M.D. Uchic, D.M. Dimiduk, A framework for automated analysis and simulation of 3D polycrystalline microstructures. Part 2: synthetic structure generation, Acta Mater. 56 (2008) 1274–1287.
[80] M.A. Groeber, M.A. Jackson, DREAM.3D: a digital representation environment for the analysis of microstructure in 3D, Integrating Mater. Manuf. Innovat. 3 (2014) 5.
[81] M. Knezevic, B. Drach, M. Ardeljan, I.J. Beyerlein, Three dimensional predictions of grain scale plasticity and grain boundaries using crystal plasticity finite element models, Comput. Meth. Appl. Mech. Eng. 277 (2014) 239–259.
[82] T.J. Barrett, D.J. Savage, M. Ardeljan, M. Knezevic, An automated procedure for geometry creation and finite element mesh generation: application to explicit grain structure models and machining distortion, Comput. Mater. Sci. 141 (2018) 269–281.
[83] M. Ardeljan, I.J. Beyerlein, M. Knezevic, Effect of dislocation density-twin interactions on twin growth in AZ31 as revealed by explicit crystal plasticity finite element modeling, Int. J. Plast. 99 (2017) 81–101.
[84] R.L. Bell, R.W. Cahn, The dynamics of twinning and the interrelation of slip and twinning in zinc crystals, Proc. Roy. Soc. Lond. Math. Phys. Sci. 239 (1957) 494–521.
[85] J. Wang, I.J. Beyerlein, C.N. Tomé, An atomic and probabilistic perspective on twin nucleation in Mg, Scripta Mater. 63 (2010) 741–746.
[86] P. Molnár, A. Jäger, P. Lejček, Twin nucleation at grain boundaries in Mg–3wt.% Al–1wt.% Zn alloy processed by equal channel angular pressing, Scripta Mater. 67 (2012) 467–470.
[87] I.J. Beyerlein, R.J. McCabe, C.N. Tomé, Effect of microstructure on the nucleation of deformation twins in polycrystalline high-purity magnesium: a multi-scale modeling study, J. Mech. Phys. Solid. 59 (2011) 988–1003.
[88] J. Wang, I.J. Beyerlein, C.N. Tomé, Reactions of lattice dislocations with grain boundaries in Mg: implications on the micro scale from atomic-scale calculations, Int. J. Plast. 56 (2014) 156–172.
[89] M.R. Barnett, S. Jacob, B.F. Gerard, J.G. Mullins, Necking and failure at low strains in a coarse-grained wrought Mg alloy, Scripta Mater. 59 (2008) 1035–1038.
[90] D. Ando, J. Koike, Y. Sutou, Relationship between deformation twinning and surface step formation in AZ31 magnesium alloys, Acta Mater. 58 (2010) 4316–4324.
[91] S. Godet, L. Jiang, A.A. Luo, J.J. Jonas, Use of Schmid factors to select extension twin variants in extruded magnesium alloy tubes, Scripta Mater. 55 (2006) 1055–1058.
[92] R. Xin, M. Wang, X. Huang, C. Guo, Q. Liu, Observation and Schmid factor analysis of multiple twins in a warm-rolled Mg–3Al–1Zn alloy, Mater. Sci. Eng. 596 (2014) 41–44.
[93] É. Martin, L. Capolungo, L. Jiang, J.J. Jonas, Variant selection during secondary twinning in Mg–3%Al, Acta Mater. 58 (2010) 3970–3983.
[94] L. Capolungo, I.J. Beyerlein, C.N. Tomé, Slip-assisted twin growth in hexagonal close-packed metals, Scripta Mater. 60 (2009) 32–35.